Control Engineering Practice 151 (2024) 106031

Contents lists available at ScienceDirect

Control Engineering Practice

journal homepage: www.elsevier.com/locate/conengprac

Model-based cascade control of single-phase Modular Multilevel Converters using ideal capacitor voltages reference

Davide Tebaldi *, Roberto Zanasi

University of Modena and Reggio Emilia, Department of Engineering Enzo Ferrari, Via Pietro Vivarelli 10, Modena, 41125, Italy

ARTICLE INFO

Keywords:
Model-based cascade control
Harmonic analysis
Modeling
Modular-multilevel converters
Power electronics
Simulation

ABSTRACT

Electrical power conversions are common in a large variety of engineering applications. With reference to AC/DC and DC/AC power conversions, a strong research interest resides in multilevel converters, thanks to the many advantages they provide over standard two-level converters. In this paper, a power-oriented model of single-phase Modular Multilevel Converters (MMCs) is first provided, followed by a detailed harmonic analysis. The model is given in the form of a Power Oriented Graphs block scheme that can be directly implemented in the Matlab/Simulink environment. The performed harmonic analysis gives a deep and exact understanding of the different terms affecting the evolution of the voltage trajectories in the upper and lower arms of the converter. Next, a new model-based cascade control architecture for MMCs is proposed. Combined with the real-time calculation of the ideal average capacitor voltages reference, the proposed control architecture allows to properly track the desired load current while minimizing the tracking error and the harmonic content in the generated load current itself.

1. Introduction

Power conversions are performed in many engineering applications, including power grids (Emin Meral & Çelik, 2020; Romero-Rodríguez et al., 2019), hybrid electric vehicles (Tebaldi & Zanasi, 2023; Zanasi & Tebaldi, 2020) and many other applications involving electric motor drives. The devices which are responsible for performing such power conversions are power converters, and can be mainly classified into DC/DC (Guo, Bahri, Diallo, & Berthelot, 2023; He, Shang, Masoud Namazi, & Ortega, 2022; Saeed, Wang, & Fernando, 2022), AC/DC and DC/AC (Cisneros et al., 2015; Kamarzarrin, Hossein Refan, & Amiri, 2022; Zanasi & Tebaldi, 2021) power converters. Multilevel converter topologies offer many pros when compared to two-level power converters (Bouarfa, Bodson, & Fadel, 2018), including distortion reduction in the output voltage waveform and in the absorbed input current as well as a reduced dv/dt effect. Different multilevel converter topologies are available in the literature, including cascaded H-bridges multilevel converters (Chiasson, Tolbert, McKenzie, & Du, 2003, 2005), converter topologies with flying capacitors (Zanasi & Tebaldi, 2021), (Hetel, Defoort, & Djemaï, 2016; Laamiri, Ghanes, & Santomenna, 2019), and Modular Multilevel Converters (MMCs) (Diaz et al., 2020)- (Montero-Robina, Marquez, Dahidah, Vazquez, Leon, Konstantinou, & Franquelo, 2022). In this paper, single-phase MMCs in half-bridge configuration are subject of study.

The first operation to be performed is a correct and accurate modeling of the considered multilevel converter topology, for which many different approaches can be found in the literature. Understanding the dynamics of the physical system to be controlled is an important aspect for a control engineer, as it helps to develop a suitable control architecture for the considered system. As an example, the dynamic model of the soybean meal drying in a industrial direct rotary dryer was derived in Luz, Dos Santos Conceição, De Matos Jorge, Paraíso, and Gonçalves Andrade (2010), based on which the proper choice of the variables to be manipulated by the controller was found. Modular Multilevel Matrix Converters are modeled in Diaz et al. (2020) in a matrix form, with the definition of a power-capacitor voltage model and of a voltage-current model. A state-space model of Modular Multilevel Converters is proposed in Liu, Li, and Yang (2020) instead. In the present paper, single-phase Modular Multilevel Converters are modeled using a new and effective approach which is based on the Power-Oriented Graphs (POG) modeling technique (Zanasi, 2010). In the literature, two additional main graphical techniques to model physical systems can be found: Bond Graphs (BG) (Badoud, Khemliche, Bacha, & Raison, 2013; Jha, Dauphin-Tanguy, & Ould-Bouamama, 2018) and Energetic Macroscopic Representation (EMR) (Delarue, Gruson, & Guillaud, 2013), (García-Herreros, Kestelyn, Gomand, Coleman, & Barre, 2013). In the present paper, the POG technique is employed as a tool

* Corresponding author.
E-mail addresses: davide.tebaldi@unimore.it (D. Tebaldi), roberto.zanasi@unimore.it (R. Zanasi).

https://doi.org/10.1016/j.conengprac.2024.106031
Received 19 May 2024; Received in revised form 16 July 2024; Accepted 17 July 2024

to develop the proposed converter model, since it provides user-friendly block schemes which are directly implementable in the Simulink environment using simple blocks available from standard libraries. Some application examples of the POG technique can be found in Zanasi and Tebaldi (2021) to model multilevel flying-capacitor converters, in Tebaldi (2022) to model Permanent Magnet Synchronous Motors and in Tebaldi and Zanasi (2020) to model multiphase diode bridge rectifiers. Two MMC models are derived in this paper: a complete model and an average model. The complete model is very suitable for a detailed simulation of the converter dynamics and provides the full differential equations describing it, whereas the average model proves to be very suitable for deriving the proposed new model-based controller of MMCs, thanks to the detailed harmonic analysis performed on it. Furthermore, a compact POG block scheme of the MMC dynamic model is proposed.

The next important step consists in properly controlling the considered multilevel converter topology. The objectives of MMC control architectures can be divided into two different parts (Steckler, Gauthier, Lin-Shi, & Wallart, 2022): the power and current control and the voltage balancing control. However, addressing all these control objectives is not an easy task. The full-order nonlinear control scheme of the MMC is addressed in Steckler et al. (2022), while a novel modulation scheme and a closed-loop method for voltage balancing allowing the fixed switching frequency of 50 Hz are proposed in Du, Liu, and Liu (2015). In Abdayem, Sawma, Khatounian, and Monmasson (2021), the authors propose a new modulation technique named Integral Modulation Technique to achieve load current control and voltage balancing, whereas a control approach based on Weighted Model Predictive Control (WMPC) for a half-bridge MMC is proposed in Ben-Brahim et al. (2016). However, this latter approach only relies on MPC to minimize an objective function to achieve both voltage balancing and load current control and does not fully analyze the complex dynamics of MMCs. A control approach based on MPC is also proposed in Riar, Geyer, and Madawala (2015), named Model Predictive Direct Current Control, proposing a cost function that also accounts for the number of switching transitions. An interesting dynamic analysis of the modular multilevel converter is proposed in Harnefors, Antonopoulos, Norrga, Ängquist, and Nee (2013) where, assuming that the output current tracks the desired profile, the nonlinear model of the MMC is derived. The system equilibrium points are then computed neglecting the oscillatory terms, based on which the control strategy of the circulating current is evinced. A new feedforward modulation technique with the objective of improving the performance in terms of modulation error in the desired arm voltage, consequently improving other aspects such as current distortion, is proposed in Montero-Robina et al. (2022). In the present paper, the following new contributions are introduced which, to the best of the authors' knowledge, have not yet been fully addressed in the literature:
(1) the development of a modeling procedure and the proposal of a compact POG block scheme modeling single-phase MMCs. The block scheme is directly implementable in the Matlab/Simulink environment using simple blocks which are available in standard Simulink libraries. Most MMC full (and average) models proposed in the literature are typically given in equations-form only (Abdayem et al., 2021; Ben-Brahim et al., 2016; Du et al., 2015; Harnefors et al., 2013; Riar et al., 2015; Steckler et al., 2022), which can become very complex and difficult to interpret and understand especially if the number of submodules, and thus switches, in the converter increases. On the other hand, the POG block scheme proposed in this paper is very compact, intuitive, easy to read and clearly highlights the power exchanges between the different parts of the system.
(2) the development of a full harmonic analysis of the system enabling a deep and exact understanding of the converter dynamics. Based on this, the circulating current reference making the average capacitor voltages track the ideal reference, that is the reference minimizing the tracking error and the harmonic content in the load current, could be determined. The detailed analytical harmonic analysis of the MMC is not addressed in other works (Abdayem et al., 2021; Ben-Brahim et al., 2016; Du et al., 2015; Riar et al., 2015; Steckler et al., 2022) or addressed in a different way for different purposes (Harnefors et al., 2013). In the latter reference, a different harmonic analysis is conducted with other objectives, including the estimation of the capacitor voltages ripple, without addressing in detail other aspects such as load current control. Furthermore, as highlighted in Harnefors et al. (2013), the sum capacitor voltage in each arm is normally desired to coincide with the pole-to-pole dc-bus voltage. In this paper, the proposed harmonic analysis allows to investigate the advantages of having a time-varying reference for the average capacitor voltages in the converter upper and lower arms, while such voltages are typically kept constant instead (Abdayem et al., 2021; Ben-Brahim et al., 2016; Du et al., 2015; Harnefors et al., 2013; Riar et al., 2015; Steckler et al., 2022). To the best of the authors' knowledge, such analysis has not been carried out in the literature yet, and leads to significant advantages as highlighted in the next point.
(3) the exact computation of the ideal voltage reference for the average capacitor voltages in the two converter arms, which is the minimum voltage strictly necessary to properly track the desired load current. The new concept of having a time-varying reference for the average capacitor voltages, which is called ideal voltage reference, proves its effectiveness in terms of reduction of the load current tracking error, as well as in terms of reduction of the load current harmonic content, when compared to the constant capacitor voltages reference case, as further discussed later on in this section.
(4) the proposal of a new model-based cascade control architecture, which allows to achieve all the benefits introduced by the new concept of ideal average capacitor voltages reference described at the previous point. The proposed architecture has two control loops: an outer voltage control loop implementing two proportional controllers, and an inner current control loop implementing an optimal current control and a voltage balancing algorithm. Using the proposed control architecture, all the control objectives are achieved at the same time: capacitor voltages balancing, tracking of the ideal average capacitor voltages reference, and tracking of the load and circulating currents. The different control objectives are typically not addressed at the same time (Harnefors et al., 2013) or addressed using MPC approaches aiming at minimizing a more complex cost function (Ben-Brahim et al., 2016). The system stability analysis is performed, and the robustness of the proposed control architecture is verified in very challenging conditions: when the load parameters needed for the proposed control architecture are fully unknown and properly identified, by considering the nonidealities such as switches on-resistances and capacitors self-discharge resistances, and considering the signals needed for the control to be affected by measurement noise.

One of the new important concepts introduced in this paper is that of ideally varying the average capacitor voltages in the converter arms exploiting the circulating current, thus proposing a new way of using the degree of freedom introduced by the circulating current itself. The ideal voltage reference is updated in real-time as a function of the desired load current and represents a crucial advantage with respect to maintaining constant average capacitor voltages, because it allows to reduce the harmonic content and the tracking error in the generated load current whenever the operating conditions allow it. This is done by minimizing the level-to-level distance in the commutating voltage signals, thus enhancing all the intrinsic main advantages of multilevel converters. The harmonic content in the load current is typically evaluated through the Total Harmonic Distortion (THD) metric (Abdayem et al., 2021; Ben-Brahim et al., 2016; Du et al., 2015). In this paper, the reduction of the load current harmonic content when using the ideal capacitor voltages reference with respect to the constant voltage reference case is quantified using different metrics, including the average value of the amplitude spectrum resulting after applying the Fast-Fourier Transform (FFT), the THD and showing the resulting amplitude spectrum.

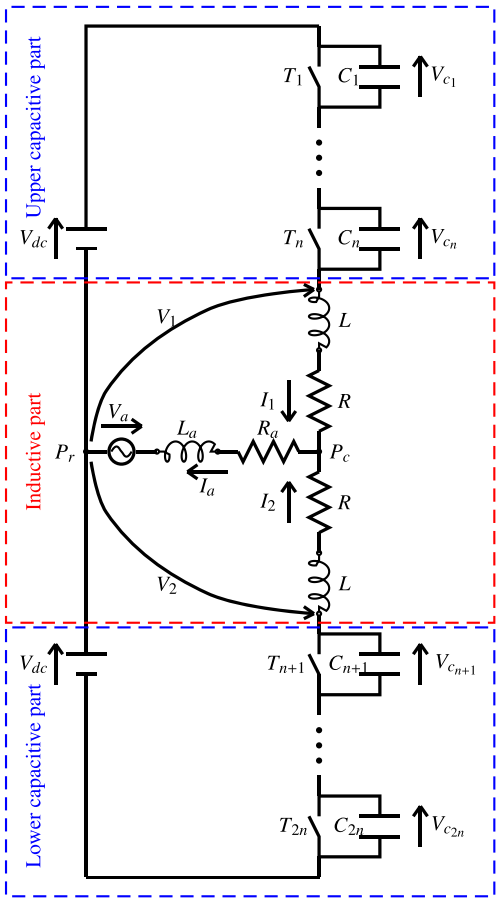

Fig. 1. Circuit diagram of the considered Modular Multilevel Converter. (For interpretation of the references to color in this figure legend, the reader is referred to the web version of this article.)

The remainder of this paper is structured as follows. Section 2 addresses the derivation of full and average dynamic models of the converter. The control problem is described and solved in Section 3, on the basis of the performed harmonic analysis and exploiting the new concept of ideal average capacitor voltages reference. Simulation results showing the effectiveness of the proposed control architecture in reducing the tracking error and the harmonic content of the load current are reported and discussed in Section 4, whereas the conclusions of this work are given in Section 5. Finally, the detailed calculations employed when performing the harmonic and stability analyses are reported in Appendices A–G.

2. Dynamic model of modular multilevel converters

The circuit diagram of a MMC with n capacitors on each arm is shown in Fig. 1, where the switches are supposed to be in half-bridge configuration. The complete dynamic model of the MMC is derived, using the POG technique, in Section 2.1 and Section 2.2 for the inductive and capacitive parts of the converter, respectively. The derivation of an average and transformed MMC dynamic model is then addressed in Section 2.3.

2.1. Dynamic model of the inductive part

The dynamic model of the inductive part of the MMC, highlighted in red in Fig. 1, can be effectively obtained starting from the expanded system shown in Fig. 2. The parameters L_1, R_1 and L_2, R_2 denote the inductances and the resistances of the upper and lower arms of the

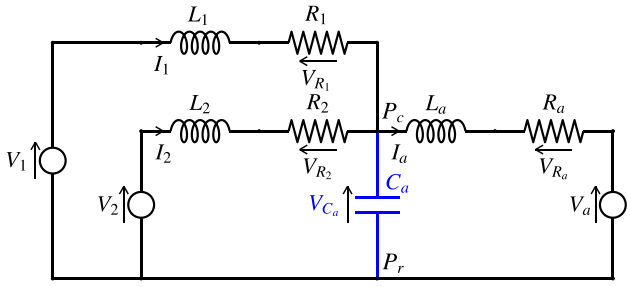

Fig. 2. Inductive part of the MMC: expanded system. (For interpretation of the references to color in this figure legend, the reader is referred to the web version of this article.)

MMC, respectively, while the parameters L_a, R_a are the load inductance and the load resistance. The variables I_2, I_1 are the arm currents, the variables V_2, V_1 are the commutating voltages defined as in Fig. 1 and V_a is a load sinusoidal voltage source. In the expanded system of Fig. 2, the system order has been augmented by introducing an additional fictitious capacitor C_a between the central point P_c and the reference point P_r, with the purpose of effectively finding the system model. The dynamics of the expanded system shown in Fig. 2 can be expressed as:

$$\underbrace{\begin{bmatrix} L_1 & 0 & 0 & 0 \\ 0 & L_2 & 0 & 0 \\ 0 & 0 & L_a & 0 \\ 0 & 0 & 0 & C_a \end{bmatrix}}_{\mathbf{L}_z} \dot{\mathbf{z}}_L = \underbrace{\begin{bmatrix} -R_1 & 0 & 0 & -1 \\ 0 & -R_2 & 0 & -1 \\ 0 & 0 & -R_a & 1 \\ 1 & 1 & -1 & 0 \end{bmatrix}}_{\mathbf{A}_z} \underbrace{\begin{bmatrix} I_1 \\ I_2 \\ I_a \\ V_{C_a} \end{bmatrix}}_{\mathbf{z}_L} + \underbrace{\begin{bmatrix} 1 & 0 \\ 0 & 1 \\ 0 & 0 \\ 0 & 0 \end{bmatrix}}_{\mathbf{B}_z} \underbrace{\begin{bmatrix} V_1 \\ V_2 \end{bmatrix}}_{\mathbf{V}_C} + \underbrace{\begin{bmatrix} 0 \\ 0 \\ -1 \\ 0 \end{bmatrix}}_{\mathbf{b}_z} V_a. \tag{1}$$

System (1) is said to be in a POG state-space form, where $\mathbf{L}_z$, $\mathbf{A}_z$ and $\mathbf{b}_z$ are the energy, power and input power matrices, respectively, which is convenient to apply congruent state-space transformations (Zanasi, 2010). When $C_a \to 0$, the constraint $I_a = I_1 + I_2$ arises from (1), generating the following congruent state-space transformation:

$$\underbrace{\begin{bmatrix} I_1 \\ I_2 \\ I_a \\ V_{C_a} \end{bmatrix}}_{\mathbf{z}_L} = \underbrace{\begin{bmatrix} 1 & 0 \\ 0 & 1 \\ 1 & 1 \\ 0 & 0 \end{bmatrix}}_{\mathbf{T}_L} \underbrace{\begin{bmatrix} I_1 \\ I_2 \end{bmatrix}}_{\mathbf{I}_L}, \tag{2}$$

where $\mathbf{I}_L$ is the new state vector. Applying (2) to system (1), and assuming $L_1 = L_2 = L$ and $R_1 = R_2 = R$, the following transformed and reduced system can be obtained:

$$\underbrace{\begin{bmatrix} L + L_a & L_a \\ L_a & L + L_a \end{bmatrix}}_{\mathbf{L}_L} \dot{\mathbf{I}}_L = -\underbrace{\begin{bmatrix} R + R_a & R_a \\ R_a & R + R_a \end{bmatrix}}_{\mathbf{A}_L} \underbrace{\begin{bmatrix} I_1 \\ I_2 \end{bmatrix}}_{\mathbf{I}_L} + \underbrace{\begin{bmatrix} V_1 \\ V_2 \end{bmatrix}}_{\mathbf{V}_C} + \underbrace{\begin{bmatrix} -1 \\ -1 \end{bmatrix}}_{\mathbf{b}_L} V_a, \tag{3}$$

where $\mathbf{L}_L = \mathbf{T}_L^{\mathrm{T}} \mathbf{L}_z \mathbf{T}_L$, $\mathbf{A}_L = \mathbf{T}_L^{\mathrm{T}} \mathbf{A}_z \mathbf{T}_L$, $\mathbf{b}_L = \mathbf{T}_L^{\mathrm{T}} \mathbf{b}_z$, $\mathbf{B}_L \mathbf{V}_C = \mathbf{V}_C$, $\mathbf{B}_L = \mathbf{T}_L^{\mathrm{T}} \mathbf{B}_z = \mathbf{I}_2$, being $\mathbf{I}_2$ the identity matrix of order 2.

2.2. Dynamic model of the capacitive part

The dynamic model of the MMC capacitive part, including the upper and lower capacitive parts highlighted in blue in Fig. 1, can be expressed as follows:

$$\begin{aligned} \underbrace{\begin{bmatrix} \mathbf{C}_1 & \mathbf{0} \\ \mathbf{0} & \mathbf{C}_2 \end{bmatrix}}_{\mathbf{L}_c} \dot{\mathbf{v}}_c &= -\underbrace{\begin{bmatrix} \mathbf{R}_{c_1}^{-1} & \mathbf{0} \\ \mathbf{0} & \mathbf{R}_{c_2}^{-1} \end{bmatrix}}_{\mathbf{R}_c^{-1}} \mathbf{v}_c + \underbrace{\begin{bmatrix} \mathbf{T}_1 & \mathbf{0} \\ \mathbf{0} & -\mathbf{T}_2 \end{bmatrix}}_{\mathbf{T}_{12}} \underbrace{\begin{bmatrix} I_1 \\ I_2 \end{bmatrix}}_{\mathbf{I}_L}, \\ \underbrace{\begin{bmatrix} V_1 \\ V_2 \end{bmatrix}}_{\mathbf{V}_C} &= -\mathbf{T}_{12}^{\mathrm{T}} \underbrace{\begin{bmatrix} \mathbf{v}_{c1} \\ \mathbf{v}_{c2} \end{bmatrix}}_{\mathbf{v}_c} - \underbrace{\begin{bmatrix} n R_{d,on} & 0 \\ 0 & n R_{d,on} \end{bmatrix}}_{\mathbf{R}_{d,on}} \underbrace{\begin{bmatrix} I_1 \\ I_2 \end{bmatrix}}_{\mathbf{I}_L} + \underbrace{\begin{bmatrix} 1 \\ -1 \end{bmatrix}}_{\mathbf{d}_c} V_{dc}, \end{aligned} \tag{4}$$

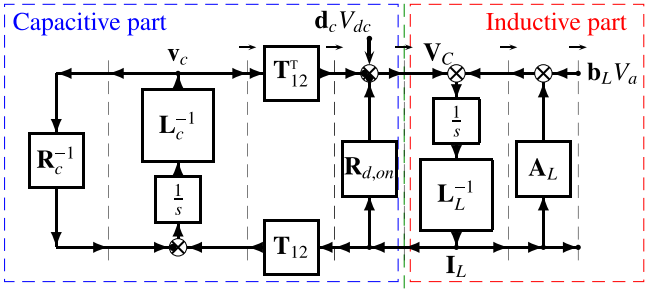

Fig. 3. POG block scheme of the complete MMC dynamic model. (For interpretation of the references to color in this figure legend, the reader is referred to the web version of this article.)

where the matrices and vectors in (4) have the following form:

$$\begin{aligned} &\mathbf{C}_1 = \mathrm{diag}(C_1, \dots, C_n), \qquad \mathbf{C}_2 = \mathrm{diag}(C_{n+1}, \dots, C_{2n}), \\ &\mathbf{R}_{c_1} = \mathrm{diag}(R_{c_1}, \dots, R_{c_n}), \qquad \mathbf{R}_{c_2} = \mathrm{diag}(R_{c_{n+1}}, \dots, R_{c_{2n}}), \\ &\mathbf{v}_{c1} = \begin{bmatrix} V_{c_1} \\ \vdots \\ V_{c_n} \end{bmatrix}, \quad \mathbf{v}_{c2} = \begin{bmatrix} V_{c_{n+1}} \\ \vdots \\ V_{c_{2n}} \end{bmatrix}, \quad \mathbf{T}_1 = \begin{bmatrix} T_1 \\ \vdots \\ T_n \end{bmatrix}, \quad \mathbf{T}_2 = \begin{bmatrix} T_{n+1} \\ \vdots \\ T_{2n} \end{bmatrix}. \end{aligned} \tag{5}$$

The parameters $R_{d,on}$ and R_{c_i} are the on-resistance of the i-th switch and the self-discharge resistance of the i-th capacitor, respectively, for $i \in \{1, 2, \dots, 2n\}$. The signals T_i are the control variables that define the state of the switches (on/off) and the use (no/yes) of the capacitors C_i in the definition of the voltages V_1 and V_2: (a) if $T_i = 0$, the i-th switch is on and the voltage V_{c_i} of capacitor C_i is not used in the Kirchhoff's Voltage Law in (4); (b) if $T_i = 1$, the i-th switch is off and the voltage V_{c_i} of capacitor C_i is used in the Kirchhoff's Voltage Law in (4). The model (3) of the MMC inductive part in Fig. 1 and the model (4) of the MMC capacitive part in Fig. 1 can be combined together to create the following complete dynamic model of the MMC:

$$\underbrace{\begin{bmatrix} \mathbf{L}_c & \mathbf{0} \\ \mathbf{0} & \mathbf{L}_L \end{bmatrix}}_{\mathbf{L}} \dot{\mathbf{x}} = \underbrace{\begin{bmatrix} -\mathbf{R}_c^{-1} & \mathbf{T}_{12} \\ -\mathbf{T}_{12}^{\mathrm{T}} & \mathbf{A}_L \end{bmatrix}}_{\mathbf{A}} \underbrace{\begin{bmatrix} \mathbf{v}_c \\ \mathbf{I}_L \end{bmatrix}}_{\mathbf{x}} + \underbrace{\begin{bmatrix} \mathbf{0} & \mathbf{0} \\ \mathbf{d}_c & \mathbf{b}_L \end{bmatrix}}_{\mathbf{B}} \underbrace{\begin{bmatrix} V_{dc} \\ V_a \end{bmatrix}}_{\mathbf{u}}, \tag{6}$$

of order $m = 2n + 2$. A very compact POG block scheme of system (6) is shown in Fig. 3. The latter is composed of elaboration and connection blocks available from the Power-Oriented Graphs technique theory described in Zanasi (2010), and has the interesting feature common to all POG block schemes, namely it can be directly implemented in the Simulink environment using simple blocks which are available in standard Simulink libraries (Zanasi, 2010). Indeed, the POG block scheme of Fig. 3 is the one implemented in the Simulink model `FULL_MMC_slx.slx` in the dataset (Tebaldi & Zanasi, 2024) using Matlab/Simulink R2023a, in order to show the implementation of the model-based control architecture proposed in this paper. The vertical black dashed lines in the POG block scheme of Fig. 3 are called power sections, describing the system power flows. The vertical green dashed line in the figure highlights the power section in correspondence of which the power flows from the capacitive part of the system to the inductive part and viceversa. The MMC model proposed in (6) and in Fig. 3 has been tested against one of the most widespread platforms for simulating power electronics systems: PLECS (Piecewise Linear Electrical Circuit Simulation) (Anon, 2024), resulting in a very good matching between the results given by the proposed MMC model in (6) and Fig. 3 and the PLECS model.

2.3. Average and transformed dynamic model

In this section, an average dynamic model of the MMC capacitive part is first derived in Section 2.3.1. Next, two congruent state-space transformations are applied to the dynamic model of the MMC inductive part and to the average dynamic model of the MMC capacitive part in Section 2.3.2, in order to derive a transformed average model.

2.3.1. Average dynamic model of the capacitive part

The order of the capacitive part (4)–(5) of the MMC dynamic model is $2n$, that is the total number of capacitors in the converter arms. Let C be the capacitance value of the capacitors in the MMC of Fig. 1. In order to have equally spaced voltage levels for voltages V_1 and V_2 in Fig. 1, the following balancing conditions must stand:

$$V_{c_1} \simeq \dots \simeq V_{c_n} \simeq \overline{V}_{c1}, \qquad V_{c_{n+1}} \simeq \dots \simeq V_{c_{2n}} \simeq \overline{V}_{c2}, \tag{7}$$

where $\overline{V}_{c1}$ and $\overline{V}_{c2}$ are the average values of the capacitors voltages in the upper and lower arms of the converter, respectively. Condition (7) can be effectively achieved using the algorithm described in Section 3.1 which is implemented every switching period T_s . If (7) holds true, the capacitive part of the MMC dynamic model (6) can be approximated using the average dynamic model derived in the remainder of this section. Assuming $R_{d,on} \to 0$ for the derivation of the average capacitive model, the variables V_1 and V_2 of vector $\mathbf{V}_C$ in (3) can only take on the following admissible voltage values:

$$\mathbf{V}_C = \begin{bmatrix} V_1 \\ V_2 \end{bmatrix} = \begin{bmatrix} V_{dc} - n_1 \overline{V}_{c1} \\ -V_{dc} + n_2 \overline{V}_{c2} \end{bmatrix}, \tag{8}$$

where the integers $n_1 \in \{0, 1, 2, \dots, n\}$ and $n_2 \in \{0, 1, 2, \dots, n\}$ denote the number of capacitors for which the corresponding switch is off in the upper and lower converter arms, i.e. for which $T_i = 1$ in Fig. 1. Assuming $R_{c_i} \to \infty$ for the derivation of the average capacitive model, the time derivative of the average voltage vector $\overline{\mathbf{V}}_c = \begin{bmatrix} \overline{V}_{c1} & \overline{V}_{c2} \end{bmatrix}^{\mathrm{T}}$ can be expressed as follows:

$$\dot{\overline{\mathbf{V}}}_c = \begin{bmatrix} \frac{d\overline{V}_{c1}}{dt} \\ \frac{d\overline{V}_{c2}}{dt} \end{bmatrix} = \begin{bmatrix} \frac{n_1 I_1}{nC} \\ -\frac{n_2 I_2}{nC} \end{bmatrix} = \frac{1}{C_T} \begin{bmatrix} n_1 I_1 \\ -n_2 I_2 \end{bmatrix}, \tag{9}$$

where $C_T = n C$. Using (8) and (9), the dynamic model of the MMC can be expressed as follows:

$$\underbrace{\begin{bmatrix} \mathbf{C}_T & \mathbf{0} \\ \mathbf{0} & \mathbf{L}_L \end{bmatrix}}_{\mathbf{L}_s} \dot{\mathbf{x}}_s = \underbrace{\begin{bmatrix} \mathbf{0} & \mathbf{A}_{12} \\ -\mathbf{A}_{12}^{\mathrm{T}} & \mathbf{A}_L \end{bmatrix}}_{\mathbf{A}_s} \underbrace{\begin{bmatrix} \overline{\mathbf{V}}_c \\ \mathbf{I}_L \end{bmatrix}}_{\mathbf{x}_s} + \underbrace{\begin{bmatrix} \mathbf{0} & \mathbf{0} \\ \mathbf{d}_c & \mathbf{b}_L \end{bmatrix}}_{\mathbf{B}_s} \underbrace{\begin{bmatrix} V_{dc} \\ V_a \end{bmatrix}}_{\mathbf{u}}, \tag{10}$$

where matrices $\mathbf{C}_T$ and $\mathbf{A}_{12}$ are defined as follows:

$$\mathbf{C}_T = \begin{bmatrix} C_T & 0 \\ 0 & C_T \end{bmatrix}, \qquad \mathbf{A}_{12} = \begin{bmatrix} n_1 & 0 \\ 0 & -n_2 \end{bmatrix}.$$

2.3.2. Transformed average model

Applying the following transformations:

$$\underbrace{\begin{bmatrix} I_1 \\ I_2 \end{bmatrix}}_{\mathbf{I}_L} = \underbrace{\frac{1}{2} \begin{bmatrix} 1 & 1 \\ 1 & -1 \end{bmatrix}}_{\mathbf{T}_w} \underbrace{\begin{bmatrix} I_s \\ I_d \end{bmatrix}}_{\mathbf{I}_w}, \qquad \underbrace{\begin{bmatrix} V_1 \\ V_2 \end{bmatrix}}_{\mathbf{V}_C} = \underbrace{\frac{1}{2} \begin{bmatrix} 1 & 1 \\ 1 & -1 \end{bmatrix}}_{\mathbf{T}_w} \underbrace{\begin{bmatrix} V_s \\ V_d \end{bmatrix}}_{\mathbf{V}_w} \tag{11}$$

to the inductive part (3) of the MMC complete model (6) yields:

$$\underbrace{\frac{1}{4} \begin{bmatrix} 2L + 4L_a & 0 \\ 0 & 2L \end{bmatrix}}_{\mathbf{L}_w} \dot{\mathbf{I}}_w = \underbrace{-\frac{1}{4} \begin{bmatrix} 2R + 4R_a & 0 \\ 0 & 2R \end{bmatrix}}_{\mathbf{A}_w} \underbrace{\begin{bmatrix} I_s \\ I_d \end{bmatrix}}_{\mathbf{I}_w} + \underbrace{\frac{1}{2} \begin{bmatrix} V_s \\ V_d \end{bmatrix}}_{\mathbf{V}_w} + \underbrace{\begin{bmatrix} -1 \\ 0 \end{bmatrix}}_{\mathbf{b}_w} V_a, \tag{12}$$

where $\mathbf{L}_w = \mathbf{T}_w^{\mathrm{T}} \mathbf{L}_L \mathbf{T}_w$, $\mathbf{A}_w = \mathbf{T}_w^{\mathrm{T}} \mathbf{A}_L \mathbf{T}_w$, $\mathbf{V}_w = \mathbf{T}_w^{\mathrm{T}} \mathbf{V}_C$ and $\mathbf{b}_w = \mathbf{T}_w^{\mathrm{T}} \mathbf{b}_L$, see Zanasi (2010). The variable I_s in (11) is the load current I_a, by applying the Kirchhoff's Current Law to the circuit diagram in Fig. 1. Hereinafter, variable I_s will be used to denote the load current I_a. The two equations of system (12) can be expanded as follows:

$$\begin{cases} L_T \dot{I}_s = -R_T I_s - 2 V_a + V_s, \\ L \dot{I}_d = -R I_d + V_d, \end{cases} \tag{13}$$

where $L_T = L + 2 L_a$ and $R_T = R + 2 R_a$. System (13) can be controlled by using the input voltages V_s and V_d introduced in (11). An important observation has to be made on system (13): the dynamics of currents I_s and I_d are *decoupled*: current I_s can only be controlled by using the input voltage V_s, whereas current I_d can only be controlled by using

the input voltage V_d. By replacing current I_s in (13) with the desired one $\tilde{I}_a$, one obtains the desired value $\tilde{V}_s$ of voltage V_s:

$$\tilde{V}_s = f(t) = L_T \dot{\tilde{I}}_a + R_T \tilde{I}_a + 2V_a. \tag{14}$$

Inverting (8) yields the following expression of the indexes n_1 and n_2:

$$\begin{bmatrix} n_1 \\ n_2 \end{bmatrix} = \begin{bmatrix} \dfrac{V_{dc} - V_1}{\overline{V}_{c1}} \\ \dfrac{V_{dc} + V_2}{\overline{V}_{c2}} \end{bmatrix}. \tag{15}$$

Substituting (15) in (9) yields the following nonlinear dynamic equations describing the capacitive part of the MMC:

$$\begin{cases} C_T \overline{V}_{c1} \dot{\overline{V}}_{c1} &= (V_{dc} - V_1) I_1, \\ C_T \overline{V}_{c2} \dot{\overline{V}}_{c2} &= -(V_{dc} + V_2) I_2. \end{cases} \tag{16}$$

Applying transformations (11) to system (16) results in:

$$\begin{cases} 4 C_T \overline{V}_{c1} \dot{\overline{V}}_{c1} &= (2V_{dc} - V_s - V_d)(I_s + I_d), \\ 4 C_T \overline{V}_{c2} \dot{\overline{V}}_{c2} &= -(2V_{dc} + V_s - V_d)(I_s - I_d). \end{cases} \tag{17}$$

The overall dynamic equations of the transformed average MMC model are given by combining together the transformed Eqs. (13) and (17) of the inductive and capacitive parts of the system, respectively.

3. Model-based control of modular multilevel converters

Control Problem. Let $\tilde{I}_a = I_{aM} \sin(\omega t)$ be the desired load current, and let $V_a = V_{aM} \sin(\omega t + \alpha_{V_a})$ be the load generator voltage source in Fig. 1. The Control Problem Goals are:
(1) Capacitor voltages control: (1.1) Maintaining the condition $V_{c_1} \simeq \cdots \simeq V_{c_n} \simeq \overline{V}_{c1}$ and $V_{c_{n+1}} \simeq \cdots \simeq V_{c_{2n}} \simeq \overline{V}_{c2}$ (capacitor voltages balancing); (1.2) Maintaining the condition $\overline{V}_{c1} \simeq \overline{V}_{c2} \simeq \overline{V}_{c12_{des}}$, where $\overline{V}_{c12_{des}}$ is the ideal average capacitor voltages reference.
(2) Load and circulating currents control: (2.1) the load current I_s must track the desired profile $\tilde{I}_a$; (2.2) the circulating current I_d must track the desired profile $\tilde{I}_d$.

The solution of Goal 1.1 of the Control Problem is addressed in Section 3.1. In Section 3.2, the transformed average MMC model in (13) and (17) is properly linearized, while the harmonic analysis on the linearized model is performed in Section 3.2.1. The computation of the desired current profile $\tilde{I}_d$ is addressed in Section 3.2.2, on the basis of the ideal average capacitor voltages reference $\overline{V}_{c12_{des}}$ computed in Section 3.2.3. Next, the discretization of the MMC model inductive part and the optimal control problem solving Goal 2.1, Goal 2.2 and Goal 1.2 of the Control Problem are discussed in Section 3.3. Section 3.4 describes the implementation and the cascade topology of the whole control architecture. Finally, the system stability analysis is carried out in Section 3.5, and Section 3.6 provides a parameters identification procedure to be used when the load parameters needed by the controller are unknown.

3.1. Solution of goal 1.1 of the control problem

The Modular Multilevel Converter of Fig. 1 is composed of n capacitors on each arm. Let $i \in \{1, \dots n\}$ and $j \in \{1, 2\}$ be the indexes identifying the $(i + (j-1)n)$-th capacitor voltage $V_{c_{i+(j-1)n}}$, where $j = 1$ identifies the upper MMC arm and $j = 2$ identifies the lower MMC arm. The Goal 1.1 of the Control Problem is achieved by implementing the algorithm schematized in Fig. 4. Other approaches in the literature aim at generating the desired arm voltage while reducing the modulation error, thus generating the load current while reducing its distortion (Montero-Robina et al., 2022). The objective of the algorithm in Fig. 4 is instead to maintain capacitor voltages balancing only. The algorithm in Fig. 4 takes as input: the index j identifying the MMC arm under consideration, the arm current I_j, the capacitor voltages vector $\mathbf{V}_{c_j}$ defined in (5), and the index n_j introduced in (8). The indexes

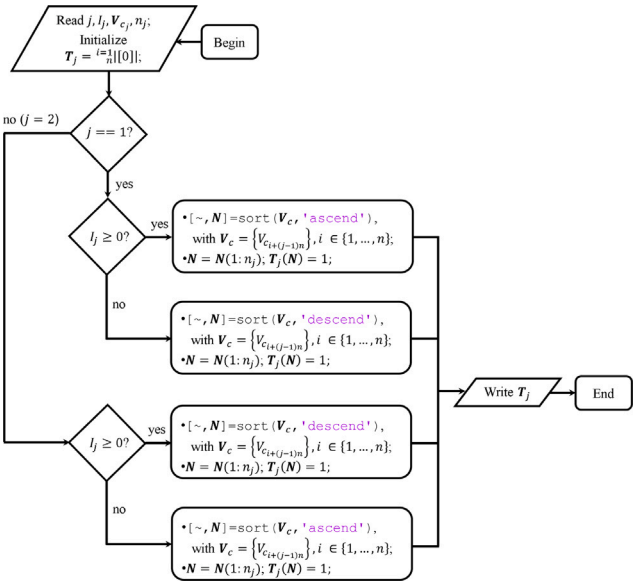

Fig. 4. Algorithm solving Goal 1.1 of the Control Problem in Section 3. (For interpretation of the references to color in this figure legend, the reader is referred to the web version of this article.)

n_j, for $j \in \{1, 2\}$, are the solution of the optimization problem (44) described in Section 3.3.1, and represent the number of capacitors involved in the generation of voltages V_j. The arm currents I_j result from the optimal control on the load and circulating currents I_s and I_d, which is addressed in Section 3.3.1. The algorithm in Fig. 4 generates as output the control vector $\mathbf{T}_j$ in the considered arm j defined in (5), and works as follows. If $j = 1$, according to the sign notations adopted in Fig. 1, a positive current $I_1 > 0$ recharges the capacitors C_i in the upper arm for which $T_i = 1$, making the corresponding voltages V_{c_i} increase. Therefore, if $j = 1$ and $I_1 > 0$, T_i is set to 1 for the n_1 capacitors having the lowest voltages V_{c_i}, where n_1 identifies the required number of capacitors to be connected in order to generate the desired voltage level V_1 in the upper arm according to (8). Conversely, if $j = 1$ and $I_1 < 0$, T_i is set to 1 for the n_1 capacitors having the highest voltages V_{c_i}. In doing so, the control vector $\mathbf{T}_1$ in (4) is determined. If $j = 2$, according to the sign notations adopted in Fig. 1, a positive current $I_2 > 0$ discharges the capacitors C_i in the lower arm for which $T_i = 1$, making the corresponding voltages V_{c_i} decrease. Therefore, the logic for sorting the capacitors to be activated is opposite with respect to the upper arm $j = 1$, in order to determine the control vector $\mathbf{T}_2$ in (4). The algorithm in Fig. 4 is executed every switching period T_s, as further discussed in Section 3.4. It can be shown that the equilibrium condition $V_{c_1} = \cdots = V_{c_n} = V_{c_{n+1}} = \cdots = V_{c_{2n}}$ is achieved if the switching frequency $f_s \to \infty$, since $I_j \neq 0$ is always verified in sinusoidal regime except for some occasional time instants. From (11) and the harmonic analysis carried out in Section 3.2.1, it can be shown that the capacitor voltages V_{c_i} never reach a constant value, but are periodical signals because of the sinusoidal nature of the arm currents I_j.

3.2. Linearization of the transformed average model

By substituting $I_s = \tilde{I}_a$ and $\tilde{V}_s$ given in (14) in the second equation of (13) and in (17), the following set of differential equations is obtained:

$$\begin{cases} L \dot{I}_d &= -R I_d + V_d, \\ 4 C_T \overline{V}_{c1} \dot{\overline{V}}_{c1} &= [2V_{dc} - V_d - f(t)](I_d + \tilde{I}_a), \\ 4 C_T \overline{V}_{c2} \dot{\overline{V}}_{c2} &= [2V_{dc} - V_d + f(t)](I_d - \tilde{I}_a). \end{cases} \tag{18}$$

The last two equations of system (18) are nonlinear with respect to variables $\overline{V}_{c1}$ and $\overline{V}_{c2}$. By introducing the substitutions $2\overline{V}_{c1} \dot{\overline{V}}_{c1} = \frac{d\overline{V}_{c1}^2}{dt} =$

$\dot{\overline{V}}^2_{c1}$ and $2\,\overline{V}_{c2}\,\dot{\overline{V}}_{c2} = \frac{d\overline{V}^2_{c2}}{dt} = \dot{\overline{V}}^2_{c2}$ in system (18), and expanding the right part, the system can be rewritten in the following form:

$$\begin{cases} L\,\dot{I}_d = -R\,I_d + V_d, \\ 2\,C_T\,\dot{\overline{V}}^2_{c1} = P_1(\omega t) + P_2(\omega t), \\ 2\,C_T\,\dot{\overline{V}}^2_{c2} = P_1(\omega t) - P_2(\omega t), \end{cases} \tag{19}$$

where the functions $P_1(\omega t)$ and $P_2(\omega t)$ have the following form:

$$\begin{aligned} P_1(\omega t) &= 2\,V_{dc}\,I_d - V_d\,I_d - f(t)\,\tilde{I}_a, \\ P_2(\omega t) &= 2\,V_{dc}\,\tilde{I}_a - V_d\,\tilde{I}_a - f(t) I_d. \end{aligned} \tag{20}$$

Systems (18) and (19) are valid for sinusoidal load current I_s and sinusoidal input voltage V_a at angular frequency ω. The last two equations of (19) are now linear with respect to variables $\overline{V}^2_{c1}$ and $\overline{V}^2_{c2}$. Note that $\dot{\overline{V}}_{c1} > 0 \Leftrightarrow \dot{\overline{V}}^2_{c1} > 0$ and viceversa. Equivalently, $\dot{\overline{V}}_{c2} > 0 \Leftrightarrow \dot{\overline{V}}^2_{c2} > 0$ and viceversa. Based on these observations, from (19) it is evident that: (a) focusing on $P_1(\omega t)$ only: when $P_1(\omega t)$ is positive, both voltages $\overline{V}_{c1}$ and $\overline{V}_{c2}$ increase as $\dot{\overline{V}}^2_{c1} > 0$ and $\dot{\overline{V}}^2_{c2} > 0$; when $P_1(\omega t)$ is negative, both voltages $\overline{V}_{c1}$ and $\overline{V}_{c2}$ decrease as $\dot{\overline{V}}^2_{c1} < 0$ and $\dot{\overline{V}}^2_{c2} < 0$. This means that function $P_1(\omega t)$ can be used to make the two voltages $\overline{V}_{c1}$ and $\overline{V}_{c2}$ follow the ideal average capacitor voltages reference $\overline{V}_{c12_{des}}$. (b) focusing on $P_2(\omega t)$ only: when $P_2(\omega t)$ is positive, voltage $\overline{V}_{c1}$ increases as $\dot{\overline{V}}^2_{c1} > 0$ and voltage $\overline{V}_{c2}$ decreases as $\dot{\overline{V}}^2_{c2} < 0$; when $P_2(\omega t)$ is negative, voltage $\overline{V}_{c1}$ decreases as $\dot{\overline{V}}^2_{c1} < 0$ and voltage $\overline{V}_{c2}$ increases as $\dot{\overline{V}}^2_{c2} > 0$. This means that function $P_2(\omega t)$ can be used to enforce the condition $\overline{V}_{c1} \simeq \overline{V}_{c2}$.

3.2.1. Harmonic analysis of the linearized model

Recalling that the desired load current $\tilde{I}_a$ and the input voltage V_a exhibit a sinusoidal behavior as in (21) and (22), the voltage V_d is designed in order to exhibit a sinusoidal behavior as well with the addition of an offset V_{d0}, as in (23):

$$\tilde{I}_a = I_{aM}\sin(\omega t), \tag{21}$$

$$V_a = V_{aM}\sin(\omega t + \alpha_{V_a}), \tag{22}$$

$$V_d = V_{d0} + V_{dM}\sin(\omega t + \alpha_{V_d}). \tag{23}$$

The design of the parameters V_{d0}, V_{dM} and α_{V_d} of voltage V_d in (23) is addressed based on the following harmonic analysis.

• *Sinusoidal behavior of function I_d:* at steady-state, when voltage V_d in (23) is applied, the solution of the first equation of system (19) is:

$$I_d = I_{d0} + I_{dM}\sin\left(\omega t + \alpha_{V_d} - \alpha_{LR}\right), \tag{24}$$

where the terms I_{d0}, I_{dM} and α_{LR} assume the following form:

$$I_{d0} = \frac{V_{d0}}{R}, \quad I_{dM} = \frac{V_{dM}}{\sqrt{R^2 + L^2\omega^2}}, \quad \alpha_{LR} = \arctan\left(\frac{L\omega}{R}\right). \tag{25}$$

• *Sinusoidal behavior of function $P_1(\omega t)$:* It can be proven, as detailed in Appendix A, that function $P_1(\omega t)$ in (20) can be written as the sum of two contributions P_{10} and $P_{1\omega}(\omega t)$ defined as:

$$\begin{cases} P_{10} = 2V_{dc}I_{d0} - V_{d0}I_{d0} - \frac{V_{dM}I_{dM}}{2}\cos(\alpha_{LR}) - \frac{f_M I_{aM}}{2}\cos(\alpha_f), \\ P_{1\omega}(\omega t) = 2\,V_{dc}\,I_{dM}\sin\left(\omega t + \alpha_{V_d} - \alpha_{LR}\right) - F_{V_d I_d}(\omega t) \\ \qquad\qquad + \frac{f_M I_{aM}}{2}\cos(2\omega t + \alpha_f), \end{cases} \tag{26}$$

where the parameters f_M and α_f are defined in Appendix D. Using (25), the constant term P_{10} in (26) can be expressed as:

$$\begin{aligned} P_{10} &= \frac{2V_{dc}V_{d0}}{R} - \frac{V_{d0}^2}{R} - \frac{V_{dM}^2}{2\sqrt{R^2+L^2\omega^2}}\cos\left(\alpha_{LR}\right) - \frac{f_M I_{aM}}{2}\cos(\alpha_f) \\ &= \frac{2V_{dc}V_{d0} - V_{d0}^2 - C_0}{R}, \end{aligned} \tag{27}$$

where the parameter C_0 is defined as follows:

$$C_0 = \frac{R\,V_{dM}^2}{2\sqrt{R^2 + L^2\omega^2}}\cos\left(\alpha_{LR}\right) + \frac{R\,f_M\,I_{aM}}{2}\cos(\alpha_f). \tag{28}$$

From (27), it is possible to verify that term P_{10} is positive if:

$$V_{d0}^- = V_{dc} - \sqrt{V_{dc}^2 - C_0} < V_{d0} < V_{dc} + \sqrt{V_{dc}^2 - C_0}. \tag{29}$$

• *Sinusoidal behavior of function $P_2(\omega t)$:* It can be proven, as detailed in Appendix C, that function $P_2(\omega t)$ in (20) can be written as the sum of two contributions P_{20} and $P_{2\omega}(\omega t)$ defined as:

$$\begin{cases} P_{20} = -\frac{V_{dM}\,I_{aM}}{2}\cos(\alpha_{V_d}) - \frac{f_M\,I_{dM}}{2}\cos(\alpha_f - \alpha_{V_d} + \alpha_{LR}), \\ P_{2\omega}(\omega t) = 2V_{dc}\,I_{aM}\sin(\omega t) - F_2(\omega t) - F_3(\omega t), \end{cases} \tag{30}$$

where the sinusoidal functions $F_2(\omega t)$ and $F_3(\omega t)$ are defined in Appendix C. After some elaboration detailed in Appendix E, the constant term P_{20} can be written as:

$$P_{20} = -\frac{V_{dM}\sqrt{a^2+b^2}}{2}\cos(\alpha_{V_d} + \gamma), \tag{31}$$

where the terms a and b are defined as:

$$a = I_{aM} + \frac{f_M\cos(\beta)}{\sqrt{R^2+L^2\omega^2}}, \qquad b = \frac{f_M\sin(\beta)}{\sqrt{R^2+L^2\omega^2}}, \tag{32}$$

and where $\beta = -\alpha_f - \alpha_{LR}$ and $\gamma = \arctan 2(b,a)$. The values of the parameters f_M, α_f and α_{LR} are given in Appendix D and (25).

Using (26) and (30) on system (19) yields:

$$\begin{cases} L\,\dot{I}_d &= -R\,I_d + V_d, \\ 2\,C_T\,\dot{\overline{V}}^2_{c1} &= P_{10} + P_{20} + P_{1\omega}(\omega t) + P_{2\omega}(\omega t), \\ 2\,C_T\,\dot{\overline{V}}^2_{c2} &= P_{10} - P_{20} + P_{1\omega}(\omega t) - P_{2\omega}(\omega t). \end{cases} \tag{33}$$

The terms $P_{1\omega}(\omega t)$ and $P_{2\omega}(\omega t)$ in (33) are the sum of sinusoidal functions at frequency ω and 2ω with zero average value. Therefore, they produce a periodic oscillation on variables $\overline{V}^2_{c1}$ and $\overline{V}^2_{c2}$ at steady-state, but they do not modify their average values. It follows that the average values of the two variables $\overline{V}^2_{c1}$ and $\overline{V}^2_{c2}$ can only be modified by the two constant terms P_{10} and P_{20}.

3.2.2. Computation of the desired circulating current $\tilde{I}_d$

Observation (1): by choosing the value $\alpha_{V_d} = -\gamma$ for the design parameter α_{V_d}, the expression of constant term P_{20} in (31) simplifies as follows:

$$P_{20} = -\frac{V_{dM}\sqrt{a^2+b^2}}{2}. \tag{34}$$

From (34), it is clear that parameter V_{dM} directly affects the value of the constant term P_{20}. Specifically, the design parameter V_{dM} has the following impact on term P_{20} and, consequently, on variables $\overline{V}_{c1}$ and $\overline{V}_{c2}$ through (33):

$$\begin{aligned} V_{dM} > 0 \;&\Rightarrow\; P_{20} < 0 \;\Rightarrow\; (\,\dot{\overline{V}}_{c1} < 0 \text{ and } \dot{\overline{V}}_{c2} > 0\,), \\ V_{dM} < 0 \;&\Rightarrow\; P_{20} > 0 \;\Rightarrow\; (\,\dot{\overline{V}}_{c1} > 0 \text{ and } \dot{\overline{V}}_{c2} < 0\,). \end{aligned} \tag{35}$$

The parameter V_{dM} can therefore be effectively exploited to enforce the condition $\overline{V}_{c1} \simeq \overline{V}_{c2}$.

Observation (2): the design parameter V_{d0} in (23) can be effectively exploited in order to make the two voltages $\overline{V}_{c1}$ and $\overline{V}_{c2}$ track the ideal average capacitor voltages reference $\overline{V}_{c12_{des}}$. Using P_{10} in (27) and C_0 in (28), it can be concluded through (29) that the design parameter V_{d0} has the following impact on term P_{10} and, through (33), on variables $\overline{V}_{c1}$ and $\overline{V}_{c2}$:

$$\begin{aligned} V_{d0} > V_{d0}^- \;&\Rightarrow\; P_{10} > 0 \;\Rightarrow\; (\,\dot{\overline{V}}_{c1} > 0 \text{ and } \dot{\overline{V}}_{c2} > 0\,), \\ V_{d0} < V_{d0}^- \;&\Rightarrow\; P_{10} < 0 \;\Rightarrow\; (\,\dot{\overline{V}}_{c1} < 0 \text{ and } \dot{\overline{V}}_{c2} < 0\,). \end{aligned} \tag{36}$$

The parameter V_{d0} can therefore be effectively exploited to increase or decrease the value of both voltages $\overline{V}_{c1}$ and $\overline{V}_{c2}$, in order for them to track the ideal average capacitor voltages reference $\overline{V}_{c12_{des}}$.

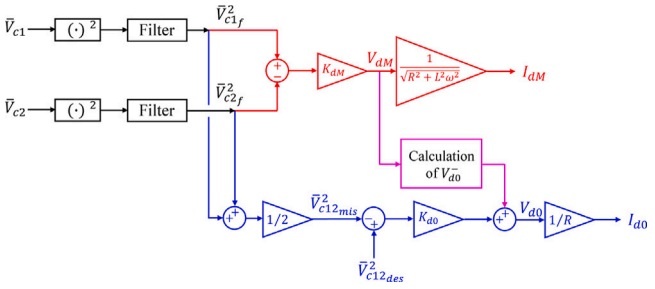

Fig. 5. Generation of the parameters I_{d0} and I_{dM} of the desired current $\tilde{I}_d$ for the control of the capacitor voltages. (For interpretation of the references to color in this figure legend, the reader is referred to the web version of this article.)

Based on the aforementioned Observations (1) and (2), the parameters I_{d0} and I_{dM} in (25) of the desired current profile $\tilde{I}_d$ having the form described in (24) are computed using the paths shown in Fig. 5.

Path 1: The first path, highlighted in red in Fig. 5, computes:

$$I_{dM} = \frac{V_{dM}}{\sqrt{R^2 + L^2\omega^2}} = \frac{K_{dM}}{\sqrt{R^2 + L^2\omega^2}}(\overline{V}^2_{c1_f} - \overline{V}^2_{c2_f}), \tag{37}$$

where $\overline{V}^2_{c1_f}$ and $\overline{V}^2_{c2_f}$ are a filtered version of the voltages $\overline{V}^2_{c1}$ and $\overline{V}^2_{c2}$. This control law, based on the choice $\alpha_{V_d} = -\gamma$, provides the value of the design parameter I_{dM} in order to enforce $\overline{V}_{c1} \simeq \overline{V}_{c2}$, and is based on relations (25) and (35).

Path 2: The second path, highlighted in blue in Fig. 5, computes:

$$I_{d0} = \frac{V_{d0}}{R} = \frac{V_{d0}^- + K_{d0}(\overline{V}^2_{c12_{des}} - \overline{V}^2_{c12_{mis}})}{R}, \qquad \overline{V}^2_{c12_{mis}} = \frac{\overline{V}^2_{c1_f} + \overline{V}^2_{c2_f}}{2}, \tag{38}$$

where V_{d0}^- is the threshold given in (29), $\overline{V}^2_{c12_{mis}}$ is the mean value of voltages $\overline{V}^2_{c1_f}$ and $\overline{V}^2_{c2_f}$, and $\overline{V}^2_{c12_{des}}$ is the ideal reference of the average capacitor voltages $\overline{V}^2_{c1}$ and $\overline{V}^2_{c2}$. Note that the error considered in (38) is $\overline{V}^2_{c12_{des}} - \overline{V}^2_{c12_{mis}}$ because system (19) is linear with respect to variables $\overline{V}^2_{c1_f}$ and $\overline{V}^2_{c2_f}$. The control law in (38) provides the value of the design parameter I_{d0} in order to make the mean of voltages $\overline{V}_{c1_f}$ and $\overline{V}_{c2_f}$ track the ideal reference $\overline{V}_{c12_{des}}$, and is based on relations (25) and (36). The part highlighted in magenta in Fig. 5 represents the calculation of parameter $V_{d0}^- = V_{d0}^-(V_{dM})$ according to (28), (29) and using the control parameter V_{dM} generated by the first path in Fig. 5.

3.2.3. Ideal average capacitor voltages reference $\overline{V}_{c12_{des}}$

The following statements hold true:

(1) From (8), smaller values for voltages $\overline{V}_{c1}$ and $\overline{V}_{c2}$ result in voltage levels $V_1 = V_{dc} - n_1\overline{V}_{c1}$ and $V_2 = -V_{dc} + n_2\overline{V}_{c2}$ which are closer to each other, thus enabling a smoother generation of voltages V_1 and V_2. In turn, this guarantees the generation of smoother currents I_1 and I_2 from (3), thus resulting in a reduction in their harmonic content. This also ensures the harmonic content reduction in the load current $I_s = I_a = I_1 + I_2$ from (11).

(2) From (8), it is possible to observe that small values for voltages $\overline{V}_{c1}$ and $\overline{V}_{c2}$ limit the lower boundary of voltage $V_1 = V_{dc} - n_1\overline{V}_{c1}$ and the upper boundary of voltage $V_2 = -V_{dc} + n_2\overline{V}_{c2}$. From (14) and recalling that $V_s = V_1 + V_2$ from (11), this may compromise the generation of the desired voltage $\tilde{V}_s$ and, consequently, of the desired load current $\tilde{I}_a$. In general, the amplitude I_{aM} and the frequency ω of the desired load current $\tilde{I}_a = \tilde{I}_a(t)$ given in (21) can be time-varying due to variations of the operating conditions, such as a fault for example, leading to variations of the desired voltage $\tilde{V}_s$ through (14). Using the desired $\tilde{I}_d$ from Fig. 5 and the first equation in (33), the desired reference $\tilde{V}_d$ for voltage V_d can be obtained. From $\tilde{V}_d$, $\tilde{V}_s$ in (14) and using (11), one obtains the desired references $\tilde{V}_1$ and $\tilde{V}_2$ for voltages V_1 and V_2:

$$\tilde{V}_1 = \frac{\tilde{V}_s + \tilde{V}_d}{2} \qquad \text{and} \qquad \tilde{V}_2 = \frac{\tilde{V}_s - \tilde{V}_d}{2}. \tag{39}$$

Let $\tilde{V}_{1M}$ and $\tilde{V}_{2M}$ denote the maximum values of the two desired voltages $\tilde{V}_1$ and $\tilde{V}_2$, and let $\tilde{V}_{12M} = (\tilde{V}_{1M} + \tilde{V}_{2M})/2$. Since $\tilde{V}_{1M} \simeq \tilde{V}_{2M}$ is desired, then $\tilde{V}_{12M} \simeq \tilde{V}_{1M} \simeq \tilde{V}_{2M}$. The ideal voltage reference $\overline{V}_{c12_{des}}$ used in Fig. 5 can be obtained from the second equation in (8) when the desired voltage $\tilde{V}_2$ takes on its maximum value $\tilde{V}_{12M}$ (i.e. when $n_2 = n$):

$$\overline{V}_{c12_{des}} = \frac{\tilde{V}_{12M} + V_{dc}}{n}. \tag{40}$$

Voltage $\overline{V}_{c12_{des}}$ in (40) satisfies the following criterion: it is the strictly minimum capacitors voltage reference allowing to generate the desired voltages $\tilde{V}_s$ and $\tilde{V}_d$, and thus the desired currents $\tilde{I}_a$ and $\tilde{I}_d$, while minimizing the level-to-level distance in voltages V_1 and V_2, thus minimizing the harmonic content in the generated load current I_s.

1. **for** $n_1(k) = n_1(k-1) - w_n : n_1(k-1) + w_n$ % cycle n_1
2. **for** $n_2(k) = n_2(k-1) - w_n : n_2(k-1) + w_n$ % cycle n_2
3. $\begin{bmatrix} V_1(k) \\ V_2(k) \end{bmatrix} = \begin{bmatrix} V_{dc} - n_1(k)\overline{V}_{c1}(k) \\ -V_{dc} + n_2(k)\overline{V}_{c2}(k) \end{bmatrix}$; % Eq. (8)
4. $\begin{bmatrix} I_1(k+1) \\ I_2(k+1) \end{bmatrix} = \begin{bmatrix} I_1(k) \\ I_2(k) \end{bmatrix} + \mathbf{L}_L^{-1}\left(\mathbf{A}_L\begin{bmatrix} I_1(k) \\ I_2(k) \end{bmatrix} + \begin{bmatrix} V_1(k) - V_a(k) \\ V_2(k) - V_a(k) \end{bmatrix}\right) T_s$ % Eq. (43)
5. $I_s(k+1) = I_1(k+1) + I_2(k+1)$; % Eq. (11)
6. $I_d(k+1) = I_1(k+1) - I_2(k+1)$; % Eq. (11)
7. $e_{I_a}(k+1) = \tilde{I}_a(k+1) - I_s(k+1)$;
8. $e_{I_d}(k+1) = I_{d_{des}}(k+1) - I_d(k+1)$;
9. **end**
10. **end**

Fig. 6. Pseudo-code for the prediction of current errors $e_{I_a}(k+1)$ and $e_{I_d}(k+1)$.

3.3. Solution of goals 1.2, 2.1 and 2.2 of the control problem

The inductive part of the MMC model in (3) can be rewritten as follows:

$$\begin{bmatrix} \dot{I}_1 \\ \dot{I}_2 \end{bmatrix} = \mathbf{L}_L^{-1}\mathbf{A}_L\begin{bmatrix} I_1 \\ I_2 \end{bmatrix} + \mathbf{L}_L^{-1}\begin{bmatrix} V_1 - V_a \\ V_2 - V_a \end{bmatrix}. \tag{41}$$

Let $I_1(k)$, $I_2(k)$ and $I_1(k+1)$, $I_2(k+1)$ be the values of currents I_1 and I_2 at the discrete time instants $t = kT_s$ and $t = (k+1)T_s$, where T_s is the sampling time. Recalling the definition of incremental ratio, it is possible to write:

$$\dot{I}_1 \approx \frac{I_1(k+1) - I_1(k)}{T_s}, \qquad \dot{I}_2 \approx \frac{I_2(k+1) - I_2(k)}{T_s}. \tag{42}$$

Replacing (42) in (41) yields the following discretized version of system (41) using the Euler's forward method:

$$\begin{bmatrix} I_1(k+1) \\ I_2(k+1) \end{bmatrix} = \begin{bmatrix} I_1(k) \\ I_2(k) \end{bmatrix} + \mathbf{L}_L^{-1}\left(\mathbf{A}_L\begin{bmatrix} I_1(k) \\ I_2(k) \end{bmatrix} + \begin{bmatrix} V_1(k) - V_a(k) \\ V_2(k) - V_a(k) \end{bmatrix}\right) T_s, \tag{43}$$

where $V_1(k)$, $V_2(k)$ and $V_a(k)$ are the values of voltages V_1, V_2 and V_a at $t = kT_s$. The Euler's forward method has been used since the prediction of the future values that the load and circulating currents assume, which is needed for the proposed optimal control problem as shown in Fig. 6 and as discussed in the next Section 3.3.1, can be effectively made using (43).

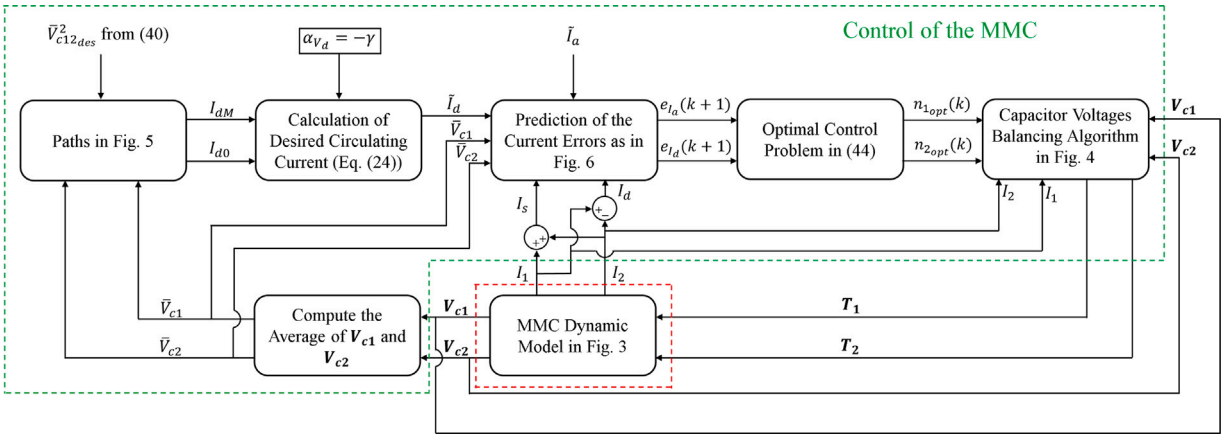

Fig. 7. Block diagram showing the implementation of the whole control architecture The control part is highlighted in green, while the modular multilevel converter is highlighted in red. (For interpretation of the references to color in this figure legend, the reader is referred to the web version of this article.)

3.3.1. Optimal control problem on currents I_a and I_d

The switching states of the modular multilevel converter in Fig. 1 are updated every T_s, being T_s the switching period. Therefore, the optimal control problem on currents I_a and I_d needs to be set up in the discrete-time domain. In the remainder of this section, the short notation "k" will be used to denote the time instant "kT_s". The output of the optimal control problem are the optimal indexes $n_1 = n_{1_{opt}}(k)$ and $n_2 = n_{2_{opt}}(k)$ to be fed to the algorithm in Fig. 4 described in Section 3.1. Let $n_1(k-1)$ and $n_2(k-1)$ be the optimal indexes given by the optimal control at the previous time step, in order to generate the voltage levels $V_1(k-1)$ and $V_2(k-1)$ according to (8), and let w_n be a window parameter that can take on discrete values from the set $\{0, \dots, n\}$. The indexes $n_1(k)$ and $n_2(k)$ can take on values such that $n_1 \in \{n_1(k-1) - w_n, \dots, n_1(k-1)+w_n\}$ and $n_2 \in \{n_2(k-1)-w_n, \dots, n_2(k-1)+w_n\}$. Note that decreasing the window w_n has the following consequences: (1) the maximum step between two consecutive voltage levels is decreased, thus emphasizing the intrinsic advantages of multilevel converters; (2) there are fewer values of $n_1(k)$ and $n_2(k)$ to choose from for the current control step, thus reducing the computational burden. When $w_n = 1$, only nine values of $n_1(k)$ and $n_2(k)$ in Fig. 6 need to be computed. Two nested "for" cycles are implemented over the possible values of $n_1(k)$ and $n_2(k)$, predicting the future errors $e_{I_a}(k+1)$ and $e_{I_d}(k+1)$ between the desired and actual load currents $\tilde{I}_a(k+1)$ and $I_s(k+1)$ and between the desired and actual circulating currents $\tilde{I}_d(k+1)$ and $I_d(k+1)$. These predictions are made for each admissible value of $n_1(k)$ and $n_2(k)$, as depicted by the pseudo-code reported in Fig. 6. The optimal indexes $n_{1_{opt}}(k)$ and $n_{2_{opt}}(k)$ are determined by solving the following optimal control problem:

$$\{n_{1_{opt}}(k), n_{2_{opt}}(k)\} = \min_{n_1(k), n_1(k)} [\alpha_1 e^2_{I_a}(k+1) + \alpha_2 e^2_{I_d}(k+1)], \tag{44}$$

where the two weights α_1 and α_2 composing the objective function in (44) satisfy the constraint $\alpha_1 + \alpha_2 = 1$. The optimal control problem (44) can be traced back to a linear Model Predictive Control (MPC) problem with a one-step prediction horizon, and can always be solved exactly thanks to the current errors prediction described in Fig. 6 and to the finite number of indexes in the two cycles at lines 1 and 2 of the pseudo-code in Fig. 6. Furthermore, problem (44) intrinsically makes the average capacitor voltages follow the desired profile $\overline{V}_{c12_{des}}$ as shown in Fig. 5, since the desired circulating current has been computed accordingly in Section 3.2.2.

3.4. Control architecture implementation and topology

The block diagram detailing the implementation of the whole control architecture is shown in Fig. 7. The complete dynamic model of the MMC in Fig. 3 is reported within the box encircled in red dashed line in Fig. 7. The control part is reported within the box encircled in green dashed line in the figure, and exploits all the concepts and calculation detailed in the previous subsections: the calculation of parameters I_{d0} and I_{dM} of the desired current profile $\tilde{I}_d$ starting from the average voltages $\overline{V}_{c1}$ and $\overline{V}_{c2}$ using the paths in Fig. 5, followed by the calculations of the desired current profile $\tilde{I}_d$ using Eqs. (24)–(25). The prediction of the future errors $e_{I_a}(k+1)$ and $e_{I_d}(k+1)$ can be made from the desired and actual load and circulating currents $\tilde{I}_a$, I_s, $\tilde{I}_d$ and I_d, where the actual currents are given by the MMC dynamic model in Fig. 3. Next, the optimal control problem in (44) gives the optimal indexes $n_{1_{opt}}(k)$ and $n_{2_{opt}}(k)$ to be fed to the capacitor voltages balancing algorithm in Fig. 4, which generates as output the control vectors $\mathbf{T}_1$ and $\mathbf{T}_2$ for the MMC dynamic model in Fig. 3. In order to make the proposed control architecture accessible by the community, the dataset (Tebaldi & Zanasi, 2024) provides a full Matlab/Simulink implementation of the whole proposed control architecture applied to the MMC complete dynamic model. The Simulink implementation of the proposed MMC model and of the proposed model-based cascade control are reported in the Simulink model `FULL_MMC_slx.slx`, which can be launched by the main script `FULL_MMC_m.m`. The provided files have been implemented in Matlab/Simulink R2023a. The block diagram showing the control structure is shown in Fig. 8. The considered control structure has a cascade topology involving two control loops and an additional feedback loop. The first control loop highlighted in red in Fig. 8 is the current control loop, and implements the optimal controller (44) on the load and circulating currents I_s and I_d in order for them to track their desired profiles $\tilde{I}_a$ and $\tilde{I}_d$ (Goals 2.1 and 2.2 of the Control Problem). The desired circulating current $\tilde{I}_d$ is generated by the action of the second feedback loop highlighted in green in Fig. 8. The latter is the voltage control loop, whose objective is to guarantee the condition $\overline{V}_{c1} \simeq \overline{V}_{c2} \simeq \overline{V}_{c12_{des}}$ (Goal 1.2 of the Control Problem), while the condition $V_{c_1} \simeq \cdots \simeq V_{c_n} \simeq \overline{V}_{c1}$, $V_{c_{n+1}} \simeq \cdots \simeq V_{c_{2n}} \simeq \overline{V}_{c2}$ (Goal 1.1 of the Control Problem) is guaranteed by the voltage balancing algorithm in Fig. 4 working at a very high switching frequency. The controllers employed in the voltage control loop of Fig. 8 are shown in Fig. 5: the proportional controller K_{dM} and the proportional controller K_{d0} plus the term V^-_{d0}. The desired voltage $\overline{V}_{c12_{des}}$ is generated through a feedforward action, which is limited to the input of the control architecture as shown by the "Feedforward Action: Eq. (14)" block in Fig. 8, and through the feedback of variable $\tilde{I}_d$ (feedback loop highlighted in blue in Fig. 8), which is one-step delayed in order to avoid the presence of an algebraic loop. The switching states of the converter are updated every switching period T_s, therefore all the control signals are sampled using the sampling time T_s through the A/D converters present in Fig. 8. The discrete-time control blocks are highlighted in light blue in Fig. 8, while the MMC continuous-time

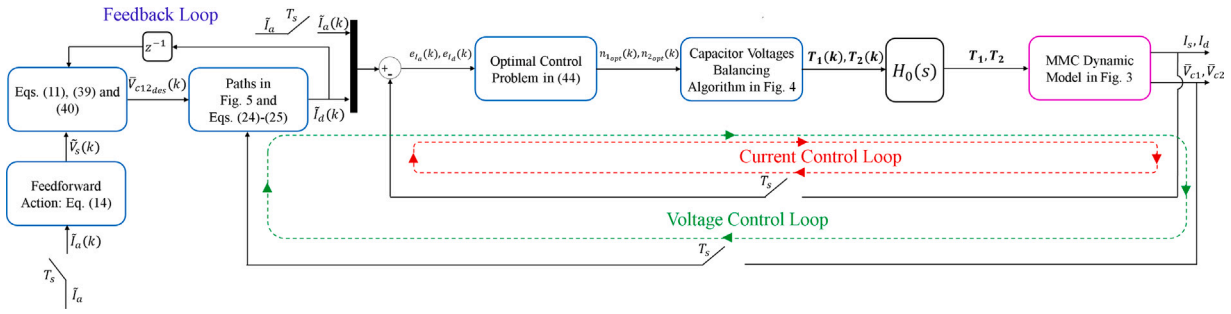

Fig. 8. Block diagram showing the cascade topology of the control architecture. The light-blue blocks are the discrete-time control blocks, while the magenta block represents the controlled system. (For interpretation of the references to color in this figure legend, the reader is referred to the web version of this article.)

dynamic model is highlighted in magenta in Fig. 8. The discrete-time control structure is executed every switching period T_s and provides the optimal sequences $\mathbf{T}_1(k) = \mathbf{T}_1(k\,T_s)$ and $\mathbf{T}_2(k) = \mathbf{T}_2(k\,T_s)$, which are then converted into the corresponding continuous-time signals $\mathbf{T}_1$ and $\mathbf{T}_2$ using the zero-order hold reconstructor.

3.5. Stability analysis

Let the following three assumptions stand:

(1) The average capacitor voltages $\overline{V}_{c1}$ and $\overline{V}_{c2}$ are sufficiently high to guarantee the asymptotic stability of the switching Current Control Loop in Fig. 8 (i.e. $I_s = \tilde{I}_a$). This assumption is justified as follows. Since the used average capacitor voltages reference $\overline{V}_{c12_{des}}$ is set to be the ideal one in (40), it means that (14), and thus $I_s = \tilde{I}_a$, can be satisfied.

(2) The dynamic behavior of the capacitor voltages $V_{c_1}, V_{c_2}, \dots, V_{c_{2n}}$ is correctly described by the average dynamic model given by the first equation of (10) or, equivalently, by the transformed differential Eqs. (17). This assumption is justified since the condition $V_{c_1} \simeq \cdots \simeq V_{c_n} \simeq \overline{V}_{c1}$ and $V_{c_{n+1}} \simeq \cdots \simeq V_{c_{2n}} \simeq \overline{V}_{c2}$ is effectively enforced by the voltage balancing algorithm of Fig. 4, which is executed at the very high switching frequency typical of the considered application.

(3) The asymptotic stability of the voltage control loop in Fig. 8 is proven starting from the last two equations of system (33) and neglecting the sinusoidal terms $P_{1\omega}(\omega t)$ and $P_{2\omega}(\omega t)$. This assumption is justified as follows. If the voltage control loop is asymptotically stable, the presence of these sinusoidal terms only causes periodical trajectories with limited amplitude in the vicinity of the stable equilibrium point.

Property 1. *The equilibrium point $\overline{V}_{c1} = \overline{V}_{c2} = \overline{V}_{c12_{des}}$ or, equivalently, $\overline{V}^2_{c1} = \overline{V}^2_{c2} = \overline{V}^2_{c12_{des}}$, is an asymptotically stable equilibrium point for the voltage control loop in Fig. 8 with a domain of attraction given by a circumference having the following radius r:*

$$r = \frac{4\sqrt{V_{dc}^2 - C_0}}{K_{do}}. \tag{45}$$

Proof. The proof is given in Appendix F.

The radius r of the domain of attraction in (45) is typically very large in practical applications, since the source voltage V_{dc} is typically very large and K_{d0} is a control parameter that can be properly designed. Indeed, using V_{dc} and K_{d0} from Table 1, the radius r of the domain of attraction is in the order of 10^6.

3.6. Parameters identification

If the load parameters L_a and R_a of the inductive part of the MMC model are unknown, they can be identified using the following moving horizon algorithm. The latter is effective in continuously updating the identification of the load parameters, thus accounting for any variation in time they might exhibit. System (3) can be rewritten as follows:

$$\begin{bmatrix} \dot{I}_a & I_a \\ \dot{I}_a & I_a \end{bmatrix} \begin{bmatrix} L_a \\ R_a \end{bmatrix} = \begin{bmatrix} V_1^a \\ V_2^a \end{bmatrix}, \tag{46}$$

where $I_a = I_1 + I_2$, $V_1^a = V_1 - V_a - \dot{I}_1 L - I_1 R$ and $V_2^a = V_2 - V_a - \dot{I}_2 L - I_2 R$. The parameters L_a and R_a of system (46) can be estimated using a least-square algorithm as $\boldsymbol{\Phi}\,\mathbf{p} = \mathbf{q}$, $\mathbf{p} = \underbrace{\boldsymbol{\Phi}^{\mathrm{T}}\boldsymbol{\Phi}^{-1}\boldsymbol{\Phi}^{\mathrm{T}}}_{\boldsymbol{\Phi}^{-\dagger}}\mathbf{q}$, where:

$$\boldsymbol{\Phi} = \begin{bmatrix} \dot{I}_a(k-1) & I_a(k-1) \\ \dot{I}_a(k-1) & I_a(k-1) \\ \dot{I}_a(k-2) & I_a(k-2) \\ \dot{I}_a(k-2) & I_a(k-2) \\ \vdots & \vdots \\ \dot{I}_a(k-N) & I_a(k-N) \\ \dot{I}_a(k-N) & I_a(k-N) \end{bmatrix}, \quad \mathbf{p} = \begin{bmatrix} L_a \\ R_a \end{bmatrix}, \quad \mathbf{q} = \begin{bmatrix} V_1^a(k-1) \\ V_2^a(k-1) \\ V_1^a(k-2) \\ V_2^a(k-2) \\ \vdots \\ V_1^a(k-N) \\ V_2^a(k-N) \end{bmatrix}, \tag{47}$$

and where the quantities $\dot{I}_a(k-i)$, $I_a(k-i)$, $V_1^a(k-i)$, $V_2^a(k-i)$ describe the corresponding variables sampled at time instant $t = (k-i)T_s$, for $i \in \{1, \dots, N\}$, being N the number of considered past samples. The identification algorithm is continuously iterated at each time instant $t = k\,T_s$, in order to continuously estimate the parameters L_a, R_a as newer samples of $\dot{I}_a$, I_a, V_1^a, V_2^a in system (46) become available. The number of past samples N represents an important degree of freedom to mitigate the impact of noise on the parameters identification.

Table 1
MMC system and controller parameters.

$L = 1$ [mH]	$R = 0.1$ [Ω]	$C_i = 1000$ [μF]
$L_a = 50$ [mH]	$R_a = 19$ [Ω]	$R_{c_i} = 50$ [kΩ]
$R_{d,on} = 1$ [mΩ]	$V_a = 10\sin(2\pi 50\,t + \frac{\pi}{6})$ [V]	$n = 8$
$V_{dc} = 250$ [V]	$T_s = 10^{-4}$ [s]	Power Factor = 0.771
$I_{aM} = 1.5, 9, 0.75$ [A]	Median filter $N_f = 200$	$K_{d0} = 0.179 \cdot 10^{-3}$
$K_{dM} = 1.5 \cdot 10^{-3}$	$\alpha_1 = 0.99,\ \alpha_2 = 0.01$	$w_n = 1$

4. Simulation results

Two simulations have been performed on the complete MMC model of Fig. 3 controlled using the architecture proposed in Fig. 8 and adopting the system and control parameters reported in Table 1. In order to simulate changes in the system operating conditions, such as for example faults, the amplitude I_{aM} of the desired load current $\tilde{I}_a$ has been chosen to vary from 1.5 A to 9 A and then to 0.75 A during the converter operation, as shown in Table 1. In the simulation of Section 4.1, the ideal reference $\overline{V}_{c12_{des}}$ computed in Section 3.2.3 is employed, whereas the simulation in Section 4.2 is performed using a constant reference $\overline{V}_{c12_{des}}$ instead, and approximately equal to the minimum value which is strictly needed to follow the desired load current $\tilde{I}_a$ during the whole simulation, which is given by the case

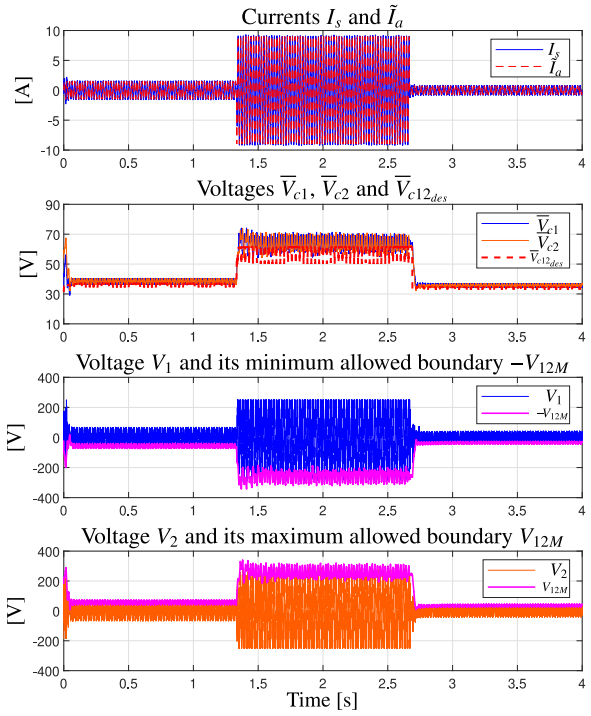

Fig. 9. Results of the first simulation. First subplot: actual and desired load currents I_s and $\tilde{I}_a$. Second subplot: actual and desired average capacitor voltages $\overline{V}_{c1}$, $\overline{V}_{c2}$ and $\overline{V}_{c12_{des}}$. Third subplot: switching voltage V_1 and its minimum allowed boundary $-V_{12M}$. Fourth subplot: switching voltage V_2 and its maximum allowed boundary V_{12M}. (For interpretation of the references to color in this figure legend, the reader is referred to the web version of this article.)

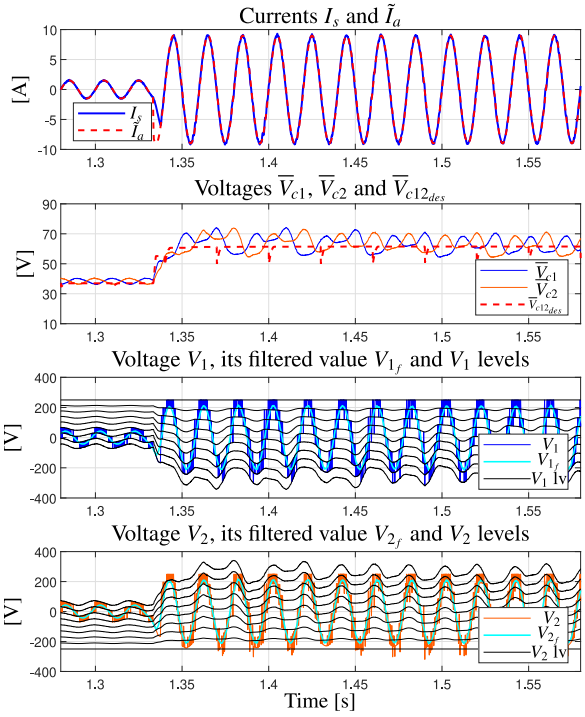

Fig. 10. Results of the first simulation: zoom-in. First subplot: actual and desired load currents I_s and $\tilde{I}_a$. Second subplot: actual and desired average capacitor voltages $\overline{V}_{c1}$, $\overline{V}_{c2}$ and $\overline{V}_{c12_{des}}$. Third subplot: switching voltage V_1, filtered voltage V_{1_f} and available levels for voltage V_1. Fourth subplot: switching voltage V_2, filtered voltage V_{2_f} and available levels for voltage V_2. (For interpretation of the references to color in this figure legend, the reader is referred to the web version of this article.)

$I_{aM} = 9$ A representing the most demanding situation. In order to consider a real scenario, measurement noise has been added to signals I_1, I_2, V_1, V_2, V_a and V_c needed by the controller. Let a be the accuracy of the considered sensor with respect to the peak range p_k, $a = 0.5\%$ and $a = 0.2\%$ are assumed for the current and voltage sensors, respectively. Given the peak amplitudes of the considered signals, sensors exhibiting the following characteristics are considered: $p_k = 10$ A for currents I_1, I_2; $p_k = 350$ V for voltages V_1, V_2; $p_k = 10$ V for voltage V_a and $p_k = 85$ V for voltages V_{c_i}. A random noise uniformly distributed between $\pm a$ of p_k has been added to the considered signals, in order to simulate signals acquisitions in a real scenario. To counteract the impact of the noise on currents I_1, I_2, a first-order filter with a time constant $\tau = 0.13 \cdot 10^{-3}$ has been employed. The initial capacitor voltages are set different from each other and range from 25 V to 62.5 V incrementing by 2.5 V for $V_{c_1}, \ldots V_{c_{16}}$, whereas the initial inductor currents are set equal to 0 A. The load parameters are supposed to be fully unknown and identified as described in Section 3.6 using $N = 1000$. The window length N_f of the median filter employed to obtain the average capacitor voltages $\overline{V}_{c1_f}$ and $\overline{V}_{c2_f}$ is computed as follows:

$$N_f = \frac{2\pi}{\omega T_s},$$

where T_s is the sampling time. The window N_f represents the number of samples contained in one period of the slowest oscillatory terms of functions $P_1(\omega t)$ and $P_2(\omega t)$ in (19). A Matlab/Simulink implementation of the proposed MMC dynamic model of Fig. 3 with the proposed control architecture of Fig. 8 is given in the files `FULL_MMC_m.m` and `FULL_MMC_slx.slx` in the dataset (Tebaldi & Zanasi, 2024) using Matlab/Simulink R2023a. The results of the first simulation are shown in Figs. 9 and 10. The results of the second simulation are shown in Figs. 11 and 12. The effective convergence of the capacitor voltages in the simulations is shown in Fig. 13, while the comparisons between the load current tracking error and harmonic content of the two simulations are shown in Fig. 14 and in Table 2.

4.1. *I simulation: Ideal capacitor voltages reference*

The results of the simulation using the ideal average capacitor voltages reference $\overline{V}_{c12_{des}}$ are shown in Figs. 9 and 10. From Fig. 9, it is possible to observe that the reference $\overline{V}_{c12_{des}}$ computed as in Section 3.2.3 is indeed the ideal one: (1) the load current I_s always tracks $\tilde{I}_a$, except for very short transients when the amplitude I_{aM} changes; (2) the lower boundary $-V_{12M}$ of voltage V_1 and the upper boundary V_{12M} of voltage V_2 always coincide with the peak value of voltages V_1 and V_2 except for the very short transients when the amplitude I_{aM} changes. The good tracking of the ideal reference $\overline{V}_{c12_{des}}$ by voltages $\overline{V}_{c1}$ and $\overline{V}_{c2}$ shown in Fig. 9, as well as the good tracking of the desired reference $\tilde{I}_a$ by the load current I_s, show the effectiveness of the Voltage and Current Control Loops in Fig. 8. In particular, the good tracking of reference $\overline{V}_{c12_{des}}$ proves the effectiveness of the control laws P_{20} and P_{10}: P_{20} keeping $\overline{V}_{c1}$ and $\overline{V}_{c2}$ as close to each other as possible and P_{10} making voltages $\overline{V}_{c1}$ and $\overline{V}_{c2}$ accurately track the varying reference $\overline{V}_{c12_{des}}$ even in correspondence of the changes in the load current amplitude. The ideal voltage reference $\overline{V}_{c12_{des}}$ is computed using (39)–(40), and represents the minimum value which is strictly needed for voltage V_s to track the desired value $\tilde{V}_s$ in (14), and for the load current I_a to track the desired value $\tilde{I}_a$. It is very convenient to make voltages $\overline{V}_{c1}$ and $\overline{V}_{c2}$ follow $\overline{V}_{c12_{des}}$ because larger $\overline{V}_{c1}$ and $\overline{V}_{c2}$ would cause the discrete voltage levels generating voltages V_1 and V_2 to be more distant from each other. As an example, Fig. 10 shows a zoom-in of Fig. 9 for $t \in [1.28,\ 1.58]$ s, showing that the transient on voltages $\overline{V}_{c1}$ and $\overline{V}_{c2}$ in correspondence of $I_{aM} = 1.5 \rightarrow 9$ A is very short. Furthermore, it is possible to observe that the available voltage

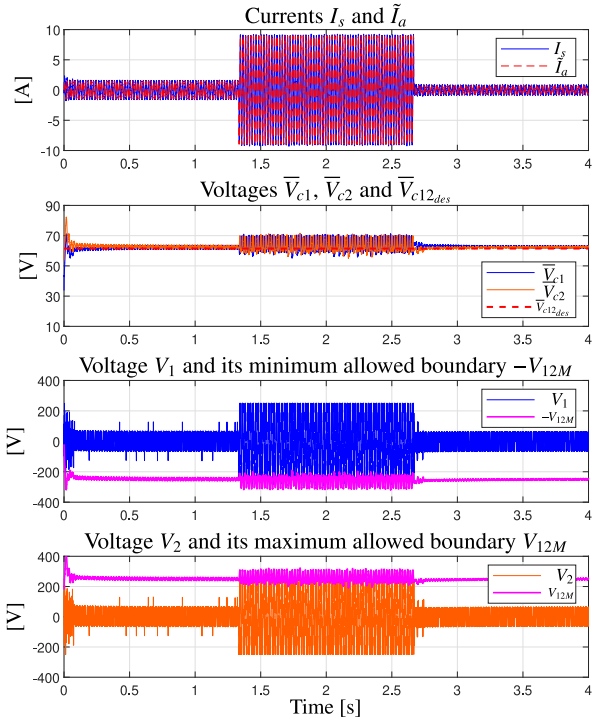

Fig. 11. Results of the second simulation. First subplot: actual and desired load currents I_s and $\tilde{I}_a$. Second subplot: actual and desired average capacitor voltages $\overline{V}_{c1}$, $\overline{V}_{c2}$ and $\overline{V}_{c12_{des}}$. Third subplot: switching voltage V_1 and its minimum allowed boundary $-V_{12M}$. Fourth subplot: switching voltage V_2 and its maximum allowed boundary V_{12M}. (For interpretation of the references to color in this figure legend, the reader is referred to the web version of this article.)

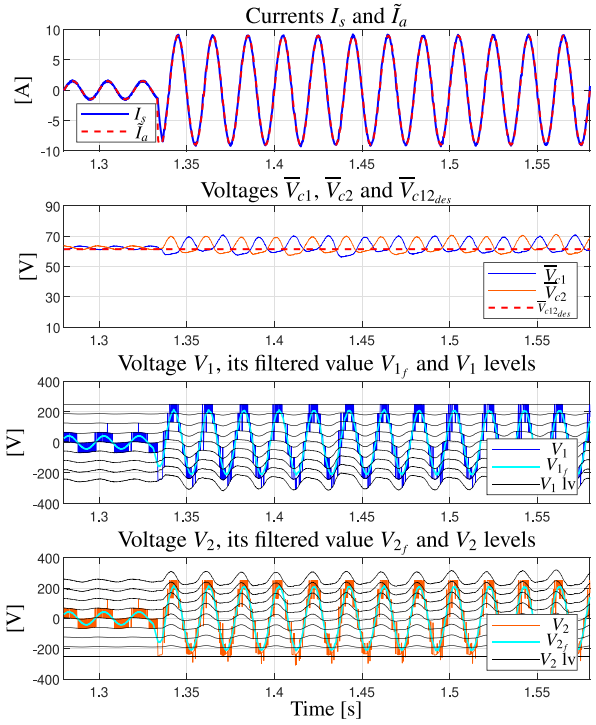

Fig. 12. Results of the second simulation: zoom-in. First subplot: actual and desired load currents I_s and $\tilde{I}_a$. Second subplot: actual and desired average capacitor voltages $\overline{V}_{c1}$, $\overline{V}_{c2}$ and $\overline{V}_{c12_{des}}$. Third subplot: switching voltage V_1, filtered voltage V_{1_f} and available levels for voltage V_1. Fourth subplot: switching voltage V_2, filtered voltage V_{2_f} and available levels for voltage V_2. (For interpretation of the references to color in this figure legend, the reader is referred to the web version of this article.)

levels (black characteristics in the figure) generating voltages V_1 and V_2 are much closer to each other whenever I_{aM} is lower. This brings two important advantages: (1) a lower harmonic content in the resulting load current I_s; (2) a better tracking of current I_s itself, leading to a cleaner sinusoid, as further discussed in Section 4.3.

4.2. II simulation: Constant capacitor voltages reference

The results of the simulation using the constant reference $\overline{V}_{c12_{des}}$ are shown in Figs. 11 and 12. In this case, the voltages $\overline{V}_{c1}$ and $\overline{V}_{c2}$ have to track the constant reference $\overline{V}_{c12_{des}}$ representing the minimum value which is strictly needed to guarantee the tracking of the desired $\tilde{I}_a$, that is the value of the ideal reference $\overline{V}_{c12_{des}}$ from the first simulation in the most demanding situation represented by the case $I_{aM} = 9$ A. Since $\overline{V}_{c12_{des}}$ is constant, Fig. 12 shows that the level-to-level distance when generating voltages V_1 and V_2 does not change throughout the simulation even when there would be room to reduce it, that is when I_{aM} decreases. This causes two main disadvantages: (1) a higher harmonic content in the resulting load current I_s; (2) a worse tracking of the load current I_s itself, as further discussed in Section 4.3.

4.3. Results comparison and discussion

This section addresses the results comparison and discussion between the two simulations in terms of capacitor voltages convergence, load current harmonic content and load current tracking error. Fig. 13 shows that the capacitor voltages V_{c_i} are effectively kept balanced and equal to the corresponding mean values $\overline{V}_{c1}$ and $\overline{V}_{c2}$ by the algorithm in Fig. 4, as well as the shortness of the voltages transients which quickly converge to the desired reference $\overline{V}_{c12_{des}}$ even when starting from different initial conditions. The comparisons between the load current tracking error and harmonic content in the two simulations are shown in Fig. 14 and in Table 2. Table 2 contains the following four metrics for comparison: the root mean square value RMS(e_{I_a}) of the load current tracking error e_{I_a}, the maximum absolute value max($|e_{I_a}|$) of the load current tracking error e_{I_a}, the average value avg(fft(I_s)) of the amplitude spectrum given by the Fast-Fourier Transform (FFT) on the load current I_s, and the load current Total Harmonic Distorsion THD(I_s). Table 2 also shows the same performances of the converter in terms of active power delivered to the load. The left subplots of Fig. 14 show the amplitude of the load current fundamental harmonic. The asterisks on the right subplots of Fig. 14 show the amplitude of the load current higher-order harmonics (i.e. at frequency greater than 50 Hz in the considered case), while the continuous lines report the average amplitude over the higher-order harmonics.

With reference to the time interval $t \in [2.14, 2.16]$ s, corresponding to one period of the load current when $I_{aM} = 9$ A, Table 2 shows that RMS(e_{I_a}) is approximately the same both in the first simulation, in which the ideal reference $\overline{V}_{c12_{des}}$ is used for voltages $\overline{V}_{c1}$ and $\overline{V}_{c2}$, and in the second simulation. This happens because the constant reference $\overline{V}_{c12_{des}}$ in the second simulation has indeed been set to the minimum value which is strictly needed to track a load current having an amplitude $I_{aM} = 9$ A. A similar observation applies to the metrics max($|e_{I_a}|$), avg(fft(I_s)) and THD(I_s). Indeed, the average amplitudes of the different higher-order harmonics in the actual load current I_s are approximately the same for both the first and the second simulations when $I_{aM} = 9$ A, see the red and blue continuous lines in the middle subplot of Fig. 14, which are very close to each other.

With reference to the time intervals $t \in [0.38, 0.4]$ s and $t \in [3.08, 3.1]$ s, corresponding to one period of the load current when $I_{aM} = 1.5$ A and $I_{aM} = 0.75$ A, respectively, Table 2 shows that RMS(e_{I_a}) and max($|e_{I_a}|$) are significantly larger in the second simulation ("Constant $\overline{V}_{c12_{des}}$" case) than in the first simulation ("Ideal varying $\overline{V}_{c12_{des}}$" case), highlighting a tracking of the desired load current profile $\tilde{I}_a$ which

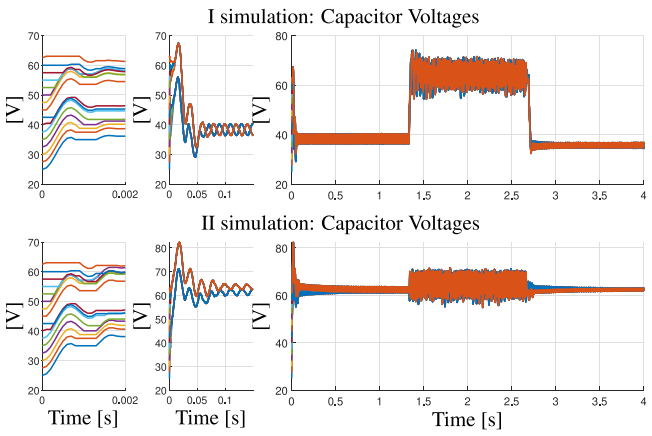

Fig. 13. Results of the first and second simulations. Right subplots: capacitor voltages V_{c_i}, for $i \in \{1, 2, \ldots, 2n\}$. Left and middle subplots: capacitor voltages V_{c_i} zoom-in. (For interpretation of the references to color in this figure legend, the reader is referred to the web version of this article.)

Table 2
Metrics evaluating the resulting load current I_s in the first and second simulation and active power.

t [s]	$t \in [0.38, 0.4]$	$t \in [2.14, 2.16]$	$t \in [3.08, 3.1]$
Constant $\overline{V}_{c12_{des}}$			
RMS(e_{I_a}) [mA]	75.09	265.9	65.65
max($\lvert e_{I_a} \rvert$) [mA]	200.9	945.9	169.3
avg(fft(I_s)) [A]	2.14	10.7	1.39
	(Ideal: 1.5)	(Ideal: 9)	(Ideal: 0.75)
THD(I_s) [dBc]	−1.05	−1.13	−0.84
Active Power [W]	21.46	762.85	5.31
Ideal $\overline{V}_{c12_{des}}$			
RMS(e_{I_a}) [mA]	56.41	252	42.14
	(**−24.88**%)		(**−35.82**%)
max($\lvert e_{I_a} \rvert$) [mA]	155.9	834.4	101.5
	(**−22.43**%)		(**−40.07**%)
avg(fft(I_s)) [A]	1.93	10.5	1.15
	(Ideal: 1.5)	(Ideal: 9)	(Ideal: 0.75)
THD(I_s) [dBc]	−1.10	−1.18	−1.21
Active Power [W]	21.45	759.67	5.23

is much worse in the second simulation. This is due to the fact that voltages V_1 and V_2 are generated using larger discrete voltage levels, as shown in Fig. 12, which in turn implies a higher harmonic content in the load current I_s, as quantified by the metrics avg(fft(I_s)) and THD(I_s) in Table 2 which are larger in the second simulation. The higher harmonic content in the load current I_s during the second simulation when $I_{aM} = 1.5$ and $I_{aM} = 0.75$ A can also be seen from the red and blue continuous lines in the upper and lower subplots of Fig. 14: the blue line is much larger than the red line, indicating a higher amplitude of the higher-order harmonics during the second simulation. This proves the effectiveness of the approach for computing the ideal average capacitor voltages reference $\overline{V}_{c12_{des}}$ and of the model-based cascade optimal controller proposed in this paper.

5. Conclusion

In this paper, the modeling, the harmonic analysis and the model-based control of MMCs using a cascade control architecture have been addressed. As far as the modeling part is concerned, a new compact POG block scheme to model single-phase MMCs has been proposed, which is directly implementable in the Matlab/Simulink environment using simple blocks that are available in standard Simulink libraries.

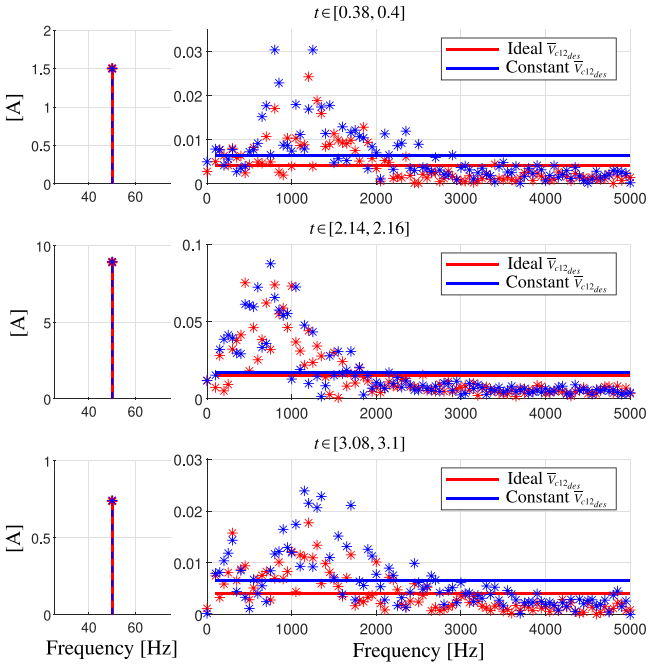

Fig. 14. Results of the first and second simulation. Right subplots: amplitude spectrum of the load current I_s at high frequencies. Left subplots: amplitude of the fundamental harmonic of the load current I_s. (For interpretation of the references to color in this figure legend, the reader is referred to the web version of this article.)

Two congruent state-space transformations have then been employed in order to decouple the MMC dynamics, thus enabling the proposed harmonic analysis of modular multilevel converters. The performed harmonic analysis has given a deep and exact understanding of the MMC dynamics. Thanks to this, the tracking reference for the circulating current in order to make the average capacitor voltages track the desired reference could be determined, and the exact computation of the ideal voltage reference for the average capacitor voltages in the upper and lower arms of the converter could be performed. Such ideal voltage reference represents the minimum value which is strictly necessary to properly track the desired load current while, at the same time, minimizing the tracking error and the harmonic content in the generated load current itself. The simulation results show that the new proposed model-based control architecture is robust even in the case where the load parameters needed for the proposed control architecture are fully unknown. The system stability analysis has been performed, and the proposed controller has been proven to be effective even in the case in which nonidealities such as switches on-resistances and capacitors self-discharge resistances are taken into account and in the case in which the signals needed for the control are affected by measurement noise. The proposed control architecture allows to effectively achieve all the goals of the Control Problem at the same time: (a) balancing of the capacitor voltages; (b) tracking of the ideal voltage reference for the average capacitor voltages in order to minimize the tracking error and the harmonic content in the load current; (c) tracking of the desired load and circulating current profiles. The simulation results also show the effectiveness of one of the new important concepts introduced in this paper, that is having time-varying average capacitor voltages in the upper and lower arms of the MMC. The circulating current is exploited in order to make the average capacitor voltages track the ideal voltage reference, which changes in real-time as a function of the desired load current. This represents a crucial advantage with respect to the classical approach of maintaining the average capacitor voltages at a constant value, because it enables the reduction of the tracking error and of the harmonic content in

the generated load current by minimizing the level-to-level distance in the commutating voltage signals, thus enhancing all the intrinsic main advantages of multilevel converters.

Funding

The work was partly supported by the University of Modena and Reggio Emilia through the action FARD (Finanziamento Ateneo Ricerca Dipartimentale) 2023–2024, and funded under the National Recovery and Resilience Plan (NRRP), Mission 04 Component 2 Investment 1.5 - NextGenerationEU, Call for tender n. 3277 dated 30/12/2021 Award Number: 0001052 dated 23/06/2022.

CRediT authorship contribution statement

Davide Tebaldi: Writing – review & editing, Writing – original draft, Visualization, Validation, Supervision, Software, Resources, Project administration, Methodology, Investigation, Funding acquisition, Formal analysis, Data curation, Conceptualization. **Roberto Zanasi:** Writing – review & editing, Writing – original draft, Visualization, Validation, Supervision, Software, Resources, Project administration, Methodology, Investigation, Funding acquisition, Formal analysis, Data curation, Conceptualization.

Declaration of competing interest

The authors declare that they have no known competing financial interests or personal relationships that could have appeared to influence the work reported in this paper.

Declaration of Generative AI and AI-assisted technologies in the writing process

During the preparation of this work the authors did not use any Generative AI and AI-assisted technologies in the writing process.

Appendix A. Sinusoidal behavior of function $P_1(\omega t)$

Function $P_1(\omega t)$ in (19) is composed of the three terms $2\,V_{dc}\,I_d$, $V_d\,I_d$ and $f(t)\tilde{I}_a$. The first term $2\,V_{dc}\,I_d$ is known, see (24). The second term $V_d\,I_d$ can be expressed as described in Appendix B. By performing the product of two sinusoidal functions, and using the expression of function $f(t)$ in Appendix D, the third term $f(t)\tilde{I}_a$ of function $P_1(\omega t)$ can be expressed as follows:

$$\begin{aligned} f(t)\tilde{I}_a &= f_M \sin(\omega t+\alpha_f) I_{aM} \sin(\omega t) \\ &= \tfrac{f_M I_{aM}}{2}\cos(\alpha_f) - \tfrac{f_M I_{aM}}{2}\cos(2\omega t+\alpha_f). \end{aligned} \tag{A.1}$$

From (14), (24), $V_d\,I_d$ in Appendix B and (A.1), it follows that function $P_1(\omega t)$ can be rewritten as in (26).

Appendix B. Sinusoidal behavior of function $V_d\,I_d$

Using (23), (24) and by performing the product of two sinusoidal functions, function $V_d\,I_d$ can be expressed as follows:

$$\begin{aligned} V_d I_d &= [V_{d0}+V_{dM}\sin(\omega t+\alpha_{V_d})]\cdot[I_{d0}+I_{dM}\sin(\omega t+\alpha_{V_d}-\alpha_{LR})] \\ &= V_{d0}I_{d0} + \tfrac{V_{dM}I_{dM}}{2}\cos(\alpha_{LR}) + F_{V_dI_d}(\omega t), \end{aligned}$$

where:

$$\begin{aligned} F_1(\omega t) &= I_{d0}\,V_{dM}\,\sin(\omega t+\alpha_{V_d}) \\ &\quad + V_{d0}\,I_{dM}\,\sin(\omega t+\alpha_{V_d}-\alpha_{LR}), \\ F_{V_dI_d}(\omega t) &= F_1(\omega t) - \tfrac{V_{dM}I_{dM}}{2}\cos(2\omega t+2\alpha_{V_d}-\alpha_{LR}) \\ &= I_{d0}V_{dM}\sin(\omega t+\alpha_{V_d}) \\ &\quad + V_{d0}I_{dM}\sin(\omega t+\alpha_{V_d}-\alpha_{LR}) \\ &\quad - \tfrac{V_{dM}I_{dM}}{2}\cos(2\omega t+2\alpha_{V_d}-\alpha_{LR}). \end{aligned} \tag{B.1}$$

Appendix C. Sinusoidal behavior of function $P_2(\omega t)$

Function $P_2(\omega t)$ in (19) is composed of the three terms $2\,V_{dc}\,\tilde{I}_a$, $V_d\,\tilde{I}_a$ and $f(t)I_d$. The first term $2V_{dc}\tilde{I}_a$ is known, see (22). By performing the product of two sinusoidal functions, the second term $V_d\,\tilde{I}_a$ can be expressed as follows:

$$\begin{aligned} V_d\tilde{I}_a &= [V_{d0}+V_{dM}\sin(\omega t+\alpha_{V_d})]I_{aM}\sin(\omega t) \\ &= \tfrac{V_{dM}I_{aM}}{2}\cos(\alpha_{V_d}) + F_2(\omega t), \end{aligned} \tag{C.1}$$

where:

$$F_2(\omega t) = V_{d0}\,I_{aM}\,\sin(\omega t) - \frac{V_{dM}\,I_{aM}}{2}\cos(2\omega t+\alpha_{V_d}).$$

By performing the product of two sinusoidal functions, the third term $f(t)\,I_d$ of function $P_2(\omega t)$ can be expressed as follows:

$$\begin{aligned} f(t)I_d &= f_M\sin(\omega t+\alpha_f)[I_{d0}+I_{dM}\sin(\omega t+\alpha_{V_d}-\alpha_{LR})] \\ &= \frac{f_M\,I_{dM}}{2}\cos(\alpha_f-\alpha_{V_d}+\alpha_{LR}) + F_3(\omega t), \end{aligned} \tag{C.2}$$

where:

$$F_3(\omega t) = I_{d0}f_M\sin(\omega t+\alpha_f) - \frac{f_M\,I_{dM}}{2}\cos(2\omega t+\alpha_f+\alpha_{V_d}-\alpha_{LR}).$$

From (14), (22), (23), (C.1) and (C.2), it follows that function $P_2(\omega t)$ can be expressed as in (30).

Appendix D. Sinusoidal behavior of function $f(t)$

Function $f(t)$ is the sum of three sinusoidal terms characterized by the same frequency ω, and can therefore be expressed as follows:

$$\begin{aligned} f(t) &= L_T\dot{\tilde{I}}_a + R_T\tilde{I}_a + 2V_a \\ &= L_T I_{aM}\omega\cos(\omega t) + R_T I_{aM}\sin(\omega t) + 2V_{aM}\sin(\omega t+\alpha_{V_a}) \\ &= f_M\,\sin(\omega t+\alpha_f), \end{aligned}$$

where:

$$f_M = \sqrt{S_f^2+C_f^2}, \qquad S_f = L_T I_{aM}\omega + 2V_{aM}\sin(\alpha_{V_a}),$$
$$\alpha_f = \arctan\left(\frac{S_f}{C_f}\right), \qquad C_f = R_T I_{aM} + 2V_{aM}\cos(\alpha_{V_a}).$$

Appendix E. The constant term P_{20}

Using (24), the constant term P_{20} can also be expressed as follows:

$$\begin{aligned} P_{20} &= -\tfrac{V_{dM}\,I_{aM}}{2}\cos(\alpha_{V_d}) - \tfrac{f_M\,I_{dM}}{2}\cos(\alpha_{V_d}-\alpha_f-\alpha_{LR}) \\ &= -\tfrac{V_{dM}}{2}a\cos(\alpha_{V_d}) + \tfrac{V_{dM}}{2}b\sin(\alpha_{V_d}) \\ &= -\tfrac{V_{dM}\sqrt{a^2+b^2}}{2}\cos(\alpha_{V_d}+\gamma), \end{aligned}$$

where $\beta = -\alpha_f - \alpha_{LR}$,

$$a = I_{aM} + \frac{f_M\cos(\beta)}{\sqrt{R^2+L^2\omega^2}} = \cos(\gamma), \qquad b = \frac{f_M\sin(\beta)}{\sqrt{R^2+L^2\omega^2}} = \sin(\gamma)$$

and $\gamma = \arctan 2(b,a)$. The values of parameters f_M and α_f have been defined in Appendix D, and the value of parameter α_{LR} has been defined in (24).

Appendix F. Proof of Property 1

Using the assumptions (1), (2), and (3) in Section 3.5, the last two equations of system (33) can be rewritten as follows:

$$\begin{cases} 4\,C_T\,\overline{V}_{c1}\,\dot{\overline{V}}_{c1} &= P_{10}+P_{20}, \\ 4\,C_T\,\overline{V}_{c2}\,\dot{\overline{V}}_{c2} &= P_{10}-P_{20}. \end{cases} \tag{F.1}$$

The two control laws P_{20} and P_{10} present in (F.1) have been proposed and defined in Section 3.2. By using Fig. 5 neglecting the filters, and using Eqs. (31), (27) and (29), the terms P_{20} and P_{10} can be expressed as follows:

$$\begin{aligned} P_{20} &= -K_1K_{dM}\left(\overline{V}_{c1}^2-\overline{V}_{c2}^2\right), \\ P_{10} &= \frac{2V_{dc}V_{d0}-V_{d0}^2-C_0}{R}, \end{aligned} \tag{F.2}$$

where:

$$\begin{aligned} K_1 &= \frac{\sqrt{a^2+b^2}}{2}\cos(\alpha_{V_d}+\gamma), \\ V_{d0} &= V_{d0}^- + K_{d0}\left(\overline{V}^2_{c12_{des}} - \frac{\overline{V}^2_{c1}+\overline{V}^2_{c2}}{2}\right). \end{aligned} \tag{F.3}$$

Let $\tilde{x}_1$ and $\tilde{x}_2$ denote the error variables defined as follows:

$$\tilde{x}_1 = \overline{V}^2_{c1} - \overline{V}^2_{c12_{des}}, \qquad \tilde{x}_2 = \overline{V}^2_{c2} - \overline{V}^2_{c12_{des}}, \tag{F.4}$$

where the reference $\overline{V}_{c12_{des}}$ is supposed to be constant. By means of (F.1), the time derivative of variables $\tilde{x}_1$ and $\tilde{x}_2$ in (F.4) can be expressed as follows:

$$\dot{\tilde{x}}_1 = 2\overline{V}_{c1}\dot{\overline{V}}_{c1} = \frac{P_{10}+P_{20}}{2C_T}, \qquad \dot{\tilde{x}}_2 = 2\overline{V}_{c2}\dot{\overline{V}}_{c2} = \frac{P_{10}-P_{20}}{2C_T}. \tag{F.5}$$

Using (F.3) and (F.4), the terms P_{20} and P_{10} in (F.2) can be rewritten as follows:

$$\begin{aligned} P_{20} &= -K_1K_{dM}\left(\tilde{x}_1-\tilde{x}_2\right), \\ P_{10} &= -a_2\left(\tilde{x}_1+\tilde{x}_2\right) - a_3\left(\tilde{x}_1+\tilde{x}_2\right)^2, \end{aligned} \tag{F.6}$$

where $a_2 = \frac{K_{d0}\sqrt{V_{dc}^2-C_0}}{R}$ and $a_3 = \frac{K_{d0}^2}{4R}$. The derivation of the expression of P_{10} in (F.6) is detailed in Appendix G. By defining the positive definite function:

$$V(\tilde{x}_1,\tilde{x}_2) = \frac{1}{2}(\tilde{x}_1^2+\tilde{x}_2^2)$$

and using (F.5) and (F.6), it follows:

$$\begin{aligned} \dot{V}(\tilde{x}_1,\tilde{x}_2) &= \tilde{x}_1\dot{\tilde{x}}_1 + \tilde{x}_2\dot{\tilde{x}}_2 \\ &= -\left(\frac{a_2+a_3(\tilde{x}_1+\tilde{x}_2)}{2C_T}\right)(\tilde{x}_1+\tilde{x}_2)^2 - \frac{K_1K_{dM}}{2C_T}(\tilde{x}_1-\tilde{x}_2)^2. \end{aligned} \tag{F.7}$$

Applying the state-space transformation $\tilde{y}_1 = \tilde{x}_1+\tilde{x}_2$, $\tilde{y}_2 = \tilde{x}_1-\tilde{x}_2$ to the last relation of (F.7) yields:

$$\dot{V}(\tilde{x}_1,\tilde{x}_2) = -\frac{a_2+a_3\tilde{y}_1}{2C_T}\tilde{y}_1^2 - \frac{K_1K_{dM}}{2C_T}\tilde{y}_2^2 \simeq -\left(\frac{a_2}{2C_T}\tilde{y}_1^2 + \frac{K_1K_{dM}}{2C_T}\tilde{y}_2^2\right) < 0, \tag{F.8}$$

from which it follows that function $\dot{V}(\tilde{x}_1,\tilde{x}_2)$ is negative definite in the vicinity of point $(\tilde{x}_1,\tilde{x}_2) = (0,0)$ since, in this region, the term $a_3(\tilde{x}_1+\tilde{x}_2)$ is negligible with respect to the constant a_2. From the Direct Lyapunov's criterion, it is possible to conclude that $(\tilde{x}_1,\tilde{x}_2) = (0,0)$ is an asymptotically stable equilibrium point for the considered second-order closed-loop system (F.1)–(F.2). From (F.4), it can be evinced that the equilibrium point $(\tilde{x}_1,\tilde{x}_2) = (0,0)$ corresponds to the condition $\overline{V}^2_{c1} = \overline{V}^2_{c2} = \overline{V}^2_{c12_{des}}$ and, therefore, to the condition $\overline{V}_{c1} = \overline{V}_{c2} = \overline{V}_{c12_{des}}$. From (F.8), it can be concluded that function $\dot{V}(\tilde{x}_1,\tilde{x}_2)$ is negative definite for all the points $(\tilde{x}_1,\tilde{x}_2)$ of the error plane satisfying the following relation:

$$\tilde{x}_1+\tilde{x}_2 > -\frac{a_2}{a_3} = -\frac{4\sqrt{V_{dc}^2-C_0}}{K_{do}} = -r. \tag{F.9}$$

The latter inequality implies that the origin $(\tilde{x}_1,\tilde{x}_2) = (0,0)$ is asymptotically stable at least in a circumference, representing the domain of attraction, having the radius r in (F.9).

Appendix G. The constant term P_{10}

Let $\tilde{x}$ denote the following error variable:

$$\tilde{x} = \overline{V}^2_{c12_{des}} - \frac{\overline{V}^2_{c1}+\overline{V}^2_{c2}}{2} = -\frac{1}{2}\left(\tilde{x}_1+\tilde{x}_2\right). \tag{G.1}$$

Using (G.1), the variable V_{d0} in (F.3) can be rewritten as follows:

$$V_{d0} = V_{d0}^- + K_{d0}\tilde{x}. \tag{G.2}$$

Using Fig. 5, (27), (29) and (G.2), and performing some algebraic steps, the term P_{10} can be rewritten as follows:

$$P_{10} = \frac{2V_{dc}V_{d0}-V_{d0}^2-C_0}{R} = \frac{2K_{d0}\sqrt{V_{dc}^2-C_0}}{R}\tilde{x} - \frac{K_{d0}^2}{R}\tilde{x}^2. \tag{G.3}$$

Substituting (G.1) in the last relation of (G.3) yields:

$$P_{10} = -\frac{K_{d0}\sqrt{V_{dc}^2-C_0}}{R}\left(\tilde{x}_1+\tilde{x}_2\right) - \frac{K_{d0}^2}{4R}\left(\tilde{x}_1+\tilde{x}_2\right)^2,$$

which is the expression of parameter P_{10} used in (F.6).

References

Abdayem, A., Sawma, J., Khatounian, F., & Monmasson, E. (2021). Control of a single phase modular multilevel converter based on a new modulation technique. In *22nd IEEE international conference on industrial technology* (pp. 10–12). http://dx.doi.org/10.1109/ICIT46573.2021.9453516.

Anon (2024). Plecs documentation:. https://www.plexim.com/products/plecs.

Badoud, A., Khemliche, M., Bacha, S., & Raison, B. (2013). Modeling and performance analysis of multilevel inverter for single-phase grid connected photovoltaic modules. In *International renewable and sustainable energy conference* (pp. 7–9). http://dx.doi.org/10.1109/IRSEC.2013.6529727.

Ben-Brahim, L., Gastli, A., Trabelsi, M., Ghazi, K.-A., Houchati, M., & Abu-Rub, H. (2016). Modular multilevel converter circulating current reduction using model predictive control. *IEEE Transactions on Industrial Electronics*, *63*(6), 3857–3866. http://dx.doi.org/10.1109/TIE.2016.2519320.

Bouarfa, A., Bodson, M., & Fadel, M. (2018). An optimization formulation of converter control and its general solution for the four-leg two-level inverter. *IEEE Transactions on Control Systems Technology*, *26*(5), 1901–1908. http://dx.doi.org/10.1109/TCST.2017.2738608.

Chiasson, J.-N., Tolbert, L.-M., McKenzie, K.-J., & Du, Z. (2003). Control of a multilevel converter using resultant theory. *IEEE Transactions on Control Systems Technology*, *11*(3), 345–354. http://dx.doi.org/10.1109/TCST.2003.810382.

Chiasson, J.-N., Tolbert, L.-M., McKenzie, K.-J., & Du, Z. (2005). Elimination of harmonics in a multilevel converter using the theory of symmetric polynomials and resultants. *IEEE Transactions on Control Systems Technology*, *13*(2), 216–223. http://dx.doi.org/10.1109/TCST.2004.839556.

Cisneros, R., Pirro, M., Bergna, G., Ortega, R., Ippoliti, G., & Molinas, M. (2015). Global tracking passivity-based PI control of bilinear systems: Application to the interleaved boost and modular multilevel converters. *Control Engineering Practice*, *43*, 109–119. http://dx.doi.org/10.1016/j.conengprac.2015.07.002.

Delarue, P., Gruson, F., & Guillaud, X. (2013). Energetic macroscopic representation and inversion based control of a modular multilevel converter. In *15th European conference on power electronics and applications* (pp. 2–6). http://dx.doi.org/10.1109/EPE.2013.6631859.

Diaz, M., Cardenas, R., Ibaceta, E., Mora, A., Urrutia, M., Espinoza, M., et al. (2020). An overview of modelling techniques and control strategies for modular multilevel matrix converters. *Energies*, *13*(18), 4678. http://dx.doi.org/10.3390/en13184678.

Du, S., Liu, J., & Liu, T. (2015). Modulation and closed-loop-based DC capacitor voltage control for MMC with fundamental switching frequency. *IEEE Transactions on Power Electronics*, *30*(1), 327–338. http://dx.doi.org/10.1109/TPEL.2014.2301836.

Emin Meral, M., & Çelik, D. (2020). Proportional complex integral based control of distributed energy converters connected to unbalanced grid system. *Control Engineering Practice*, *103*, http://dx.doi.org/10.1016/j.conengprac.2020.104574.

García-Herreros, I., Kestelyn, X., Gomand, J., Coleman, R., & Barre, P.-J. (2013). Model-based decoupling control method for dual-drive gantry stages: a case study with experimental validations. *Control Engineering Practice*, *21*(3), 298–307. http://dx.doi.org/10.1016/j.conengprac.2012.10.010.

Guo, Q., Bahri, I., Diallo, D., & Berthelot, E. (2023). Model predictive control and linear control of DC-DC boost converter in low voltage DC microgrid: An experimental comparative study. *131*, http://dx.doi.org/10.1016/j.conengprac.2022.105387.

Harnefors, L., Antonopoulos, A., Norrga, S., Ängquist, L., & Nee, H.-P. (2013). Dynamic analysis of modular multilevel converters. *IEEE Transactions on Industrial Electronics*, *60*(7), 2526–2537. http://dx.doi.org/10.1109/TIE.2012.2194974.

He, W., Shang, Y., Masoud Namazi, M., & Ortega, R. (2022). Adaptive sensorless control for buck converter with constant power load. *Control Engineering Practice*, *126*, http://dx.doi.org/10.1016/j.conengprac.2022.105237.

Hetel, L., Defoort, M., & Djemaï, M. (2016). Binary control design for a class of bilinear systems: application to a multilevel power converter. *IEEE Transactions on Control Systems Technology*, *24*(2), 719–726. http://dx.doi.org/10.1109/TCST.2015.2460696.

Jha, M.-S., Dauphin-Tanguy, G., & Ould-Bouamama, B. (2018). Robust fault detection with interval valued uncertainties in bond graph framework. *Control Engineering Practice*, *71*, 61–78. http://dx.doi.org/10.1016/j.conengprac.2017.10.009.

Kamarzarrin, M., Hossein Refan, M., & Amiri, P. (2022). Open-circuit faults diagnosis and Fault-Tolerant Control scheme based on Sliding-Mode Observer for DFIG back-to-back converters: wind turbine applications. *Control Engineering Practice*, *126*, http://dx.doi.org/10.1016/j.conengprac.2022.105235.

Laamiri, S., Ghanes, M., & Santomenna, G. (2019). Observer based direct control strategy for a multi-level three phase flying-capacitor inverter. *Control Engineering Practice*, *86*, 155–165. http://dx.doi.org/10.1016/j.conengprac.2019.03.011.

Liu, M., Li, Z., & Yang, X. (2020). A universal mathematical model of modular multilevel converter with half-bridge. *Energies*, *13*(17), 4464. http://dx.doi.org/10.3390/en13174464.

Luz, G. R., Dos Santos Conceição, W. A., De Matos Jorge, L. M., Paraíso, P. R., & Gonçalves Andrade, C. M. (2010). Dynamic modeling and control of soybean meal drying in a direct rotary dryer. *Food and Bioproducts Processing*, *88*(2–3), 90–98. http://dx.doi.org/10.1016/j.fbp.2010.01.008.

Montero-Robina, P., Marquez, A., Dahidah, M. S. A., Vazquez, S., Leon, J. I., Konstantinou, G., et al. (2022). Feedforward modulation technique for more accurate operation of modular multilevel converters. *IEEE Transactions on Power Electronics*, *37*(2), 1700–1710. http://dx.doi.org/10.1109/TPEL.2021.3104984.

Riar, B. S., Geyer, T., & Madawala, U. K. (2015). Model predictive direct current control of modular multilevel converters: modeling, analysis, and experimental evaluation. *IEEE Transactions on Power Electronics*, *30*(1), 431–439. http://dx.doi.org/10.1109/TPEL.2014.2301438.

Romero-Rodríguez, M., Delpoux, R., Piétrac, L., Dai, J., Benchaib, A., & Niel, E. (2019). An implementation method for the supervisory control of time-driven systems applied to high-voltage direct current transmission grids. *Control Engineering Practice*, *82*, 97–107. http://dx.doi.org/10.1016/j.conengprac.2018.10.002.

Saeed, J., Wang, L., & Fernando, N. (2022). Model predictive control of phase shift full-bridge DC-DC converter using laguerre functions. *IEEE Transactions on Control Systems Technology*, *30*(2), 819–826. http://dx.doi.org/10.1109/TCST.2021.3069148.

Steckler, P.-B., Gauthier, J.-Y., Lin-Shi, X., & Wallart, F. (2022). Differential flatness-based, full-order nonlinear control of a modular multilevel converter (MMC). *IEEE Transactions on Control Systems Technology*, *30*(2), 547–557. http://dx.doi.org/10.1109/TCST.2021.3067887.

Tebaldi, D. (2022). Efficiency map-based PMSM parameters estimation using power-oriented modeling. *IEEE Access*, *10*, 45954–45961. http://dx.doi.org/10.1109/ACCESS.2022.3169149.

Tebaldi, D., & Zanasi, R. (2020). Modeling and simulation of a multiphase diode bridge rectifier. In *IEEE European control conference* (pp. 12–15). http://dx.doi.org/10.23919/ECC51009.2020.9143693.

Tebaldi, D., & Zanasi, R. (2023). Systematic modeling of complex time-variant gear systems using a Power-Oriented approach. *Control Engineering Practice*, *132*, http://dx.doi.org/10.1016/j.conengprac.2022.105420.

Tebaldi, D., & Zanasi, R. (2024). Model-based control of modular multilevel converters, Mendeley data, V2. http://dx.doi.org/10.17632/j4875x8jxw.2, https://data.mendeley.com/datasets/j4875x8jxw/2.

Zanasi, R. (2010). The power-oriented graphs technique: system modeling and basic properties. In *Proceedings of IEEE vehicle power and propulsion conference* (pp. 1–3). http://dx.doi.org/10.1109/VPPC.2010.5729018.

Zanasi, R., & Tebaldi, D. (2020). Modeling of complex planetary gear sets using power-oriented graphs. *IEEE Transactions on Vehicular Technology*, *69*(12), 14470–14483. http://dx.doi.org/10.1109/TVT.2020.3040899.

Zanasi, R., & Tebaldi, D. (2021). Modeling control and robustness assessment of multilevel flying-capacitor converters. *Energies*, *14*(7), 1903. http://dx.doi.org/10.3390/en14071903.